

# An experimental scaling law for particle-size segregation in dense granular flows

T. Trehwela<sup>1,†</sup>, C. Ancey<sup>1</sup> and J.M.N.T. Gray<sup>2</sup>

<sup>1</sup>École Polytechnique Fédérale de Lausanne, Écublens 1015 Lausanne, Switzerland

<sup>2</sup>Department of Mathematics and Manchester Centre for Nonlinear Dynamics, University of Manchester, Oxford Road, Manchester M13 9PL, UK

(Received 15 June 2020; revised 31 January 2021; accepted 11 March 2021)

Particles of differing sizes are notoriously prone to segregation in shear driven flows under the action of gravity. This has important implications in many industrial processes, where particle-size segregation can lead to flow problems and reduced product quality, as well as longer product development and start-up times. Particle-size segregation also readily occurs in many hazardous geophysical mass flows (such as snow avalanches, debris flows and volcanic pyroclastic flows) and can lead to the formation of destructive bouldery flow fronts and significantly longer runouts. Although general theories exist to model particle-size segregation, the detailed functional dependence of the segregation flux on the shear rate, gravity, pressure, particle concentration, grain size and grain-size ratio is still not known. This paper describes refractive-index matched oscillatory shear-cell experiments that shed light on the segregation velocity in the two extreme cases of (i) a single large intruder rising up through a matrix of smaller grains, and (ii) a single small intruder percolating down through a matrix of large particles. Despite the sometimes markedly different time scales for segregation in these two situations, a unifying scaling law has been found that is able to collapse all the experimental data over a wide range of shear rates and grain-size ratios in the range [1.17, 4.17]. The resulting functional form is easily generalizable to intermediate concentrations and can quantitatively capture laboratory experiments and numerical simulations with a 50 : 50 mix of large and small grains.

**Key words:** granular media, particle/fluid flow

† Email address for correspondence: [tomas.trehwela@epfl.ch](mailto:tomas.trehwela@epfl.ch)

© The Author(s), 2021. Published by Cambridge University Press. This is an Open Access article, distributed under the terms of the Creative Commons Attribution licence (<http://creativecommons.org/licenses/by/4.0/>), which permits unrestricted re-use, distribution, and reproduction in any medium, provided the original work is properly cited.

## 1. Introduction

Shallow granular free-surface flows (or granular avalanches) are one of the most common particle transport mechanisms in industrial bulk solids handling processes. They form in chute flows (Savage & Hutter 1989; Gray, Wieland & Hutter 1999), as well as in thin fluid-like layers at the free surface of heaps (Williams 1968; Baxter *et al.* 1998; Fan *et al.* 2012), silos (Bates 1997; Schulze 2008; Liu, Gonzalez & Wassgren 2019; Isner *et al.* 2020) and rotating tumblers (Gray & Hutter 1997; Hill *et al.* 1999; Khakhar, Orpe & Hajra 2003; Schlick *et al.* 2015; Gilberg & Steiner 2020). These high density, gravity driven, shear flows are highly efficient at segregating particles by size. Despite many years of research, particle-size segregation continues to present considerable practical problems in many industrial processes (Johanson 1978; Isner *et al.* 2020). Sometimes the segregation is useful, such as in the mining industry (Wills 1979). However, in the bulk chemical, pharmaceutical, agricultural and food industries it is the single biggest cause of product non-uniformity (Bates 1997). This can lead to complete product batches having to be discarded at significant cost. In addition, the evolving local particle-size distribution may feedback on the rheology of the bulk flow and cause unexpected flow problems (Pouliquen, Delour & Savage 1997; Pouliquen & Vallance 1999; Baker, Johnson & Gray 2016) that are still poorly understood. Segregation-induced frictional feedback is also thought to play a vital part in the formation of bouldery flow fronts (Pierson 1986; Denissen *et al.* 2019) and static levees (Iverson & Vallance 2001; Baker *et al.* 2016; Rocha, Johnson & Gray 2019) in geophysical mass flows (such as snow avalanches, debris flows and pyroclastic flows), which can significantly enhance their run out.

In the avalanching region of these industrial and geophysical flows, small grains percolate towards the base of the shearing layer and large grains rise towards the free surface. Complex interactions between the shear flow and an underlying static, or slowly moving region of grains, can lead to the development of amazing patterns in the deposit (e.g. Williams 1968; Gray & Hutter 1997; Baxter *et al.* 1998; Hill *et al.* 1999; Barker *et al.* 2021). However, for a steady-state flow on a fixed base, an inversely graded particle-size distribution develops, with the large particles concentrated at the top of the flow and the finer grains concentrated near the base. The segregation occurs due to the combination of two processes; kinetic sieving (Middleton 1970) and squeeze expulsion (Savage & Lun 1988). Essentially, as the layers of grains shear past one another they act as random fluctuating sieves, which preferentially allow small particles to percolate downwards into gaps that open up beneath them (known as kinetic sieving), while all particles are squeezed upwards with equal probability (known as squeeze expulsion), which maintains an approximately constant solid volume fraction (GDR-MiDi 2004). This has been termed gravity driven segregation (Gray 2018) for short, to reflect the fact that gravity is fundamental to the smaller grains falling into the gaps between the larger grains, and therefore setting the direction for segregation. The grains also diffuse within the shear flow, which produces a smoothly varying inversely graded particle-size distribution at steady state (with the large grains concentrated on top of the fines) rather than being sharply segregated.

The earliest continuum model for bidisperse particle segregation was developed by Bridgwater, Foo & Stephens (1985). It consists of a spatially one-dimensional time-dependent advection–diffusion equation, with a shear-rate-dependent segregation flux that shuts off when the species concentration reaches zero and one hundred per cent. The key elements of this theory are still present in more recent multi-dimensional models that use either a quadratic (e.g. Savage & Lun 1988; Dolgunin & Ukolov 1995; Khakhar *et al.* 2003; Gray & Thornton 2005; Gray & Chugunov 2006; Thornton, Gray & Hogg

2006; Gray & Ancey 2011; Wiederseiner *et al.* 2011; Tripathi & Khakhar 2013; Gajjar & Gray 2014; Tunuguntla, Bokhove & Thornton 2014; Gray & Ancey 2015; Schlick *et al.* 2015; Xiao *et al.* 2016; Liu *et al.* 2019; Gilberg & Steiner 2020) or cubic (e.g. Gajjar & Gray 2014; van der Vaart *et al.* 2015; Jones *et al.* 2018) small particle concentration dependence in the segregation flux.

Wiederseiner *et al.* (2011) filmed the spatially two-dimensional steady-state segregation of large black and small white particles through the sidewall of a chute. By using a calibration curve, they were able to determine the local small particle concentrations as the grains segregated from a sharply segregated normally graded inflow (with all the small particles on top of the large grains) to a fully developed inversely graded steady state. Wiederseiner *et al.* (2011) showed that by using the measured downslope velocity, and choosing appropriate constant values for the segregation velocity magnitude and the diffusivity, it was possible to accurately model the spatial development of the concentration using Gray & Chugunov's (2006) theory. Thornton *et al.* (2012) performed discrete particle model (DPM) simulations in a periodic box using bidisperse mixtures of particles with different size ratios. The final steady-state numerical results were then compared to the exact steady-state solution of Gray & Chugunov (2006). In this solution the length scale for the transition between high concentrations of large and small particles, is inversely proportional to the Péclet number for segregation. This is defined as the flow thickness times the segregation velocity magnitude divided by the diffusivity. Thornton *et al.* (2012) showed that the Péclet number increased with increasing grain-size ratio and peaked at a value close to 8 at a grain-size ratio just below two. However, Wiederseiner *et al.* (2011) found experimental values of the Péclet number between 11 and 19 for similar size ratios. This discrepancy may be due to the coupling with the bulk velocity, which was an exponential profile in Wiederseiner *et al.*'s (2011) experiments, but was Bagnold-like (Silbert *et al.* 2001) in Thornton *et al.*'s (2012) simulations, since they are not affected by sidewall friction.

In order to better visualize the segregation in experiments, van der Vaart *et al.* (2015) performed a series of refractive-index matched particle-size segregation experiments in an oscillating shear box. This has the advantage that the shear rate is independent of depth, and the flow field is explicitly prescribed rather than spontaneously developing in a chute flow. The experiment was stopped after each complete oscillation and the three-dimensional particle-size distribution was determined by scanning a laser sheet across the cell while taking a series of photographs. From these extremely detailed data, van der Vaart *et al.* (2015) showed that there was a fundamental asymmetry to particle-size segregation. In particular, a single small intruder will percolate down through a matrix of large grains much faster than a single large intruder will rise up through a matrix of fines. This suggests that the segregation flux function is not quadratic, but has a more cubic-like dependence on the small particle concentration (Bridgwater *et al.* 1985; Gajjar & Gray 2014; van der Vaart *et al.* 2015; Jones *et al.* 2018).

The annular shear-cell experiments of Golick & Daniels (2009) also provide important insights into the functional dependence of the segregation flux. The experiment was driven by a moving bottom plate, but the top plate was also free to move vertically in response to the pressure generated during the flow. Their experiments showed that there were subtle packing effects, as a normally graded initial configuration mixed and then segregated into a final inversely graded steady state. The ability of the grains to pack tighter together in a shearing bidisperse mixture caused the top plate to drop from its initial height, and then recover as the particles segregated again. Intriguingly, Golick & Daniels (2009) showed that when a weight was placed on the top plate the rate of segregation was

dramatically decreased. This suggests that the segregation velocity magnitude is pressure and/or solids volume fraction dependent. This has been investigated further by Fry *et al.* (2019) using DPM simulations of a confined shear flow. Their simulations suggest that the percolation velocity, and hence the segregation velocity magnitude, is proportional to the reciprocal of the square root of the pressure. It follows that segregation is suppressed in Golick & Daniels' (2009) experiments, when a weight is applied, because the pressure reduces the segregation rate while having no effect on the diffusion.

A definitive form for the segregation flux function that makes sense of, and hopefully unifies, all the observations is still lacking. It is clear that it is dependent on the shear rate (Bridgwater *et al.* 1985; Savage & Lun 1988; May *et al.* 2010; Fan *et al.* 2014), the pressure (Golick & Daniels 2009; Fry *et al.* 2019), gravity (Vallance & Savage 2000; Gray & Thornton 2005; Gray & Chugunov 2006; Fry *et al.* 2019), the mean particle size (Fry *et al.* 2019; Chassagne *et al.* 2020) and the particle size ratio (Savage & Lun 1988; Gray & Thornton 2005; Thornton *et al.* 2012; Fan *et al.* 2014), as well as that it has a non-quadratic concentration dependence (Bridgwater *et al.* 1985; Gajjar & Gray 2014; van der Vaart *et al.* 2015; Jones *et al.* 2018). However, there may also be additional functional dependencies on the friction of the grains (Guillard, Forterre & Pouliquen 2016; Jing, Kwok & Leung 2017) and the evolving local solids volume fraction (Golick & Daniels 2009; Gilberg & Steiner 2020).

This paper aims to shed further light on the functional form of the segregation flux by using refractive-index matched shear-cell experiments and dimensional analysis. Section 2 reviews the governing equations and explains the rationale behind studying the extreme end states of a single large, and a single small, intruder. Section 3 describes the experimental shear box and the refractive-index matching technique. Section 4 uses dimensional analysis and a series of key observations to motivate a simple functional form for the flux. Sections 5 and 6 compare the theoretical large and small intruder trajectories to those measured in experiment, for a wide range of shear rates and size ratios, and show that the data can be collapsed using the same non-dimensional coefficients. Section 7 shows that the theory quantitatively matches van der Vaart *et al.*'s (2015) shear box experiments with a 50 : 50 mix of particles using the same non-dimensional coefficients and the simplest possible function to map between the size-ratio dependence of the large and small intruders. Section 8 introduces the concept of increased packing efficiency as the grain-size ratio becomes large and discusses how this is able to moderate the overall segregation. Section 9 then concludes and makes some interesting observations about the functional form of the segregation flux that is implied by the theory.

## 2. Bidisperse particle-size segregation

### 2.1. Governing equations

Consider a mixture of large and small particles whose pore space is occupied by an interstitial fluid. Each of the constituents occupies a volume fraction  $\Phi^v \in [0, 1]$  per unit mixture volume, where the constituent letters  $v = l, s$  and  $f$ , refer to large particles, small particles and fluid, respectively. It is also possible to define volume fractions of large and small particles per unit granular volume

$$\phi^l = \frac{\Phi^l}{\Phi^l + \Phi^s}, \quad \phi^s = \frac{\Phi^s}{\Phi^l + \Phi^s}. \quad (2.1a,b)$$

This is useful, because in many situations of practical interest the solids volume fraction  $\Phi = \Phi^l + \Phi^s$  does not change very much (Silbert *et al.* 2001; GDR-MiDi 2004) and can

therefore be scaled out of the equations (Thornton *et al.* 2006). In this situation, the general form of the bidisperse segregation equations for the volume fractions (concentrations) of the large and small particles (see e.g. Gray 2018) are

$$\frac{\partial \phi^l}{\partial t} + \nabla \cdot (\phi^l \mathbf{u}) - \nabla \cdot \left( f_{sl} \phi^l \phi^s \frac{\mathbf{g}}{|\mathbf{g}|} \right) = \nabla \cdot (\mathcal{D}_{sl} \nabla \phi^l), \quad (2.2)$$

$$\frac{\partial \phi^s}{\partial t} + \nabla \cdot (\phi^s \mathbf{u}) + \nabla \cdot \left( f_{sl} \phi^s \phi^l \frac{\mathbf{g}}{|\mathbf{g}|} \right) = \nabla \cdot (\mathcal{D}_{sl} \nabla \phi^s), \quad (2.3)$$

respectively, where  $\mathbf{u}$  is the bulk granular velocity field,  $f_{sl}$  is the segregation velocity magnitude,  $\mathbf{g}$  is the gravitational acceleration vector and  $\mathcal{D}_{sl}$  is the diffusivity of the large and small particles. Since by definition the concentration of large and small particles sum to unity

$$\phi^l + \phi^s = 1, \quad (2.4)$$

the sum of (2.2) and (2.3) implies that the bulk velocity field is incompressible

$$\nabla \cdot \mathbf{u} = 0. \quad (2.5)$$

This is reasonable leading-order approximation that is made in the incompressible  $\mu(I)$ -rheology (GDR-MiDi 2004; Jop, Forterre & Pouliquen 2006; Barker & Gray 2017) for example (where  $\mu$  is the friction and  $I$  is the inertial number). It should be noted, however, that in reality there is some compressibility and indeed compressibility is needed to make the rheology thermodynamically consistent (Goddard & Lee 2018) and well posed (Barker *et al.* 2017; Schaeffer *et al.* 2019). In this paper, however, the solids volume fraction is assumed to be equal to a constant uniform value of  $\Phi = 0.6$ .

## 2.2. Segregation fluxes and velocities

In (2.2) and (2.3) the large and small particle segregation fluxes are

$$\mathbf{F}^l = -f_{sl} \phi^l \phi^s \frac{\mathbf{g}}{|\mathbf{g}|}, \quad (2.6)$$

$$\mathbf{F}^s = +f_{sl} \phi^s \phi^l \frac{\mathbf{g}}{|\mathbf{g}|}, \quad (2.7)$$

respectively. These are aligned with the direction of gravitational acceleration  $\mathbf{g}$  to reflect the fact that the downward percolation of small particles due to kinetic sieving is a gravity driven process. In order to maintain bulk incompressibility there is a net reverse flow of large particles towards the surface due to squeeze expulsion. In the absence of diffusion the segregation velocity of the large and small particles relative to the bulk flow are

$$\hat{\mathbf{u}}^l = \mathbf{u}^l - \mathbf{u} = -f_{sl} \phi^s \frac{\mathbf{g}}{|\mathbf{g}|}, \quad (2.8)$$

$$\hat{\mathbf{u}}^s = \mathbf{u}^s - \mathbf{u} = +f_{sl} \phi^l \frac{\mathbf{g}}{|\mathbf{g}|}, \quad (2.9)$$

respectively. The summation constraint (2.4) implies that the segregation fluxes (2.6)–(2.7) are zero when either of the particle species is in a pure phase. If  $f_{sl}$  is independent of  $\phi^s$  and  $\phi^l$  then (2.4) implies that the large particle segregation flux is quadratic in  $\phi^s$  and is symmetric about  $\phi^s = 1/2$ . Equation (2.8) shows that the corresponding large particle segregation velocity is linear in  $\phi^s$  and hence implies that the maximum segregation

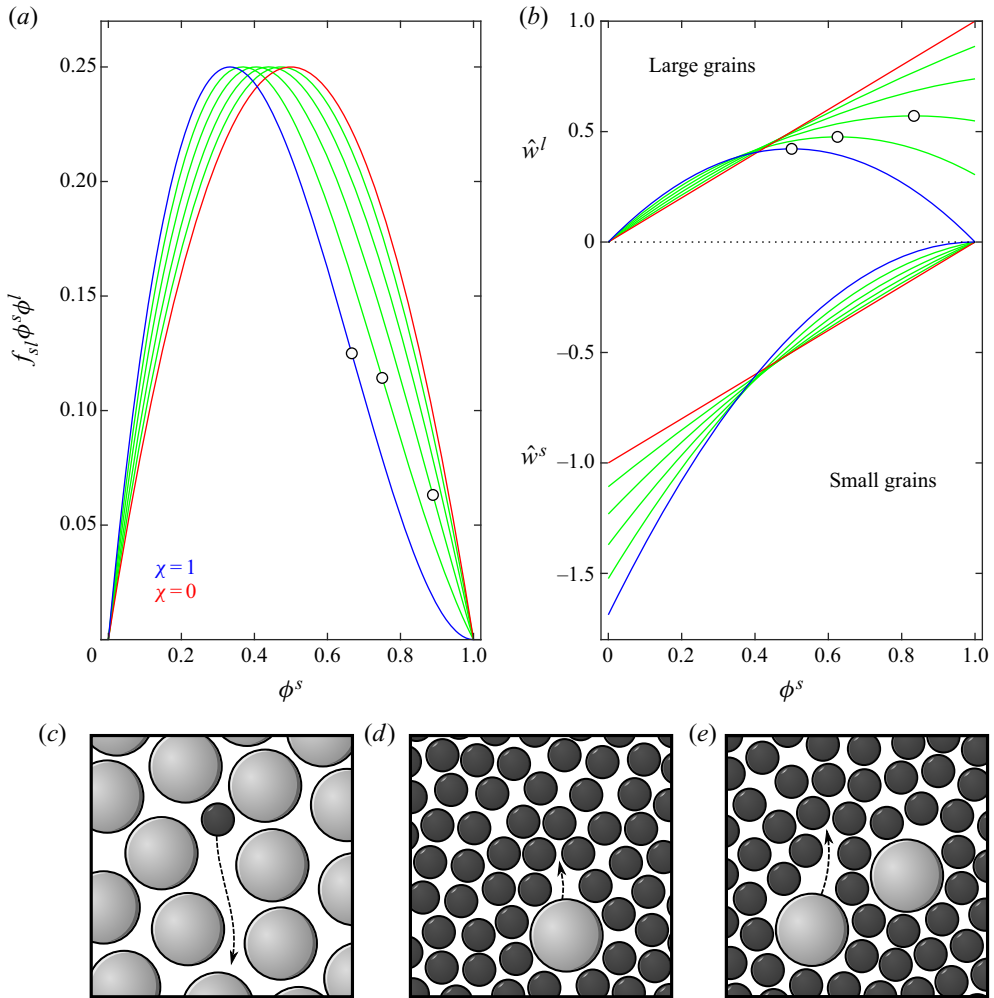


Figure 1. (a) Segregation flux functions and (b) the large and small particle segregation velocities as a function of the small particle concentration  $\phi^s$  (adapted from Gajjar & Gray 2014; Gray 2018). These assume that  $f_{sl} = A_\chi (1 - \chi \phi^s)$ , where  $\chi \in [0, 1]$  and  $A_\chi$  is a normalization factor giving all the flux functions the same amplitude as the quadratic flux when  $\chi = 0$  (red lines). The blue lines show the cubic flux model of Bridgwater *et al.* (1985) for  $\chi = 1$  and the green lines show the intermediate cases when  $\chi = 0.2, 0.4, 0.6, 0.8$ . For  $\chi \in [1/2, 1]$  these develop an inflection point at  $\phi_{inf}^s = (1 + \chi)/(3\chi)$  (circular markers a) and a group of large particles rise fastest at  $\phi_{crit}^s = 1/(2\chi)$  (circular markers b). Sketches showing (c) the rapid percolation of a single small intruder in a matrix of large grains, (d) the slow rise of a single large particle in a matrix of fine and (e) the faster rise of a group of large particles at intermediate concentrations for a sufficiently skewed flux function.

velocity is equal to  $f_{sl}$  and is attained when there is a single large grain at concentration  $\phi^s = 1^-$  (note the superscript minus is used to show that the concentration is not 100 % small particles, i.e. there is a large intruder, but it does not significantly change the local concentration from unity). Similarly, the small particle segregation velocity is linear in  $\phi^l$  and the maximum segregation velocity equals  $-f_{sl}$  and is attained when there is a single small grain at concentration  $\phi^s = 0^+$ . The quadratic large particle segregation flux function and the associated linear segregation velocities are plotted in figure 1(a,b).

Using shear box experiments van der Vaart *et al.* (2015) showed that there was an underlying asymmetry to the particle-size segregation, i.e. a single small particle

percolating down through a matrix of large particles moves much faster than a single large particle being squeezed up through a matrix of fines. This is illustrated schematically in [figure 1\(c,d\)](#) and is not captured in the simple quadratic flux model. Gajjar & Gray (2014) showed that this asymmetry could, however, be captured by skewing the peak segregation flux towards smaller concentrations of fine grains, as illustrated for a cubic flux function in [figure 1\(a\)](#). As the peak of the large particle segregation flux moves to the left, the maximum downward small particle segregation velocity (at  $\phi^s = 0^+$ ) is progressively increased even though the maximum amplitude of the flux function stays the same. As the cubic flux curves become skewed, the large particle segregation velocity at concentration  $\phi^s = 1^-$  is progressively diminished below that of the quadratic flux model. Moreover, as the skewness parameter  $\chi$  rises above one half, an inflection point develops in the flux function and the maximum segregation velocity of large particles no longer occurs at  $\phi^s = 1^-$ , but at an intermediate concentration  $\phi^s$  within the range  $[1/2, 1]$ . As a result a group of large particles will rise faster than an individual large intruder as illustrated schematically in [figure 1\(d,e\)](#).

The theory shows that studying (i) a large intruder being squeezed up through a matrix of fine particles and (ii) a small intruder percolating down through a matrix of large grains can yield a considerable amount of information about the shape of the segregation flux function. A series of single-intruder refractive-index matched shear box experiments have therefore been performed in this paper.

### 3. Refractive-index matched shear box experiments

#### 3.1. Experimental apparatus

The shear box apparatus is shown in [figure 2\(a\)](#). It consists of two polyvinyl chloride (PVC) rough lateral side plates that are able to pivot about two transverse steel rods, that are located at their centres and bolted to glass panes at the front and back of the shear box. The top ends of the PVC plates are attached to a steel bar that keeps the plates parallel and connects them to a horizontally moving plunger driven by a rotational motor. The bottom of the sheared domain consists of another rough PVC plate of length  $L = 4.5$  cm, which sets the distance between the two rotating walls, and is free to move horizontally within slotted grooves in the transparent front and back walls. As the top of the PVC side plates are driven backwards and forwards the plates pivot about their centres and push the base plate from side to side as shown in [figure 2\(b\)](#). To try to prevent the formation of crystalline particle structures the three PVC plates have a random stepped roughness profile, whose average length and depth are of the scale of the background particles. For instance, in the experiment shown in [figure 2](#) the average profile length and depth are 4 mm and 2 mm, respectively, and the background medium size is  $d_s = 6$  mm. To give structural stability the four corners of the glass panes were screwed to steel spacer tubes to maintain the transverse separation width  $W = 7$  cm of the shear cell. The volume between the three PVC plates is filled to a height  $h = 12$  cm with a mixture of large and small borosilicate glass beads of diameter  $d_l$  and  $d_s$ , respectively. The whole cell is then submerged in a refractive-index matched fluid to make the semi-opaque intruder easy to identify and track. All the materials used to make the box were selected to be compliant with the refractive index matching technique. The dimensions of the shear cell have been selected to impose a slightly dilated bulk shearing motion on all the grains in the cell. Earlier prototypes had a larger separation distance between the pivoting walls that allowed crystalline particle packings to develop in regions of the flow, which is undesired. A relatively small spacing between the two rotating walls appears to prevent such effects.

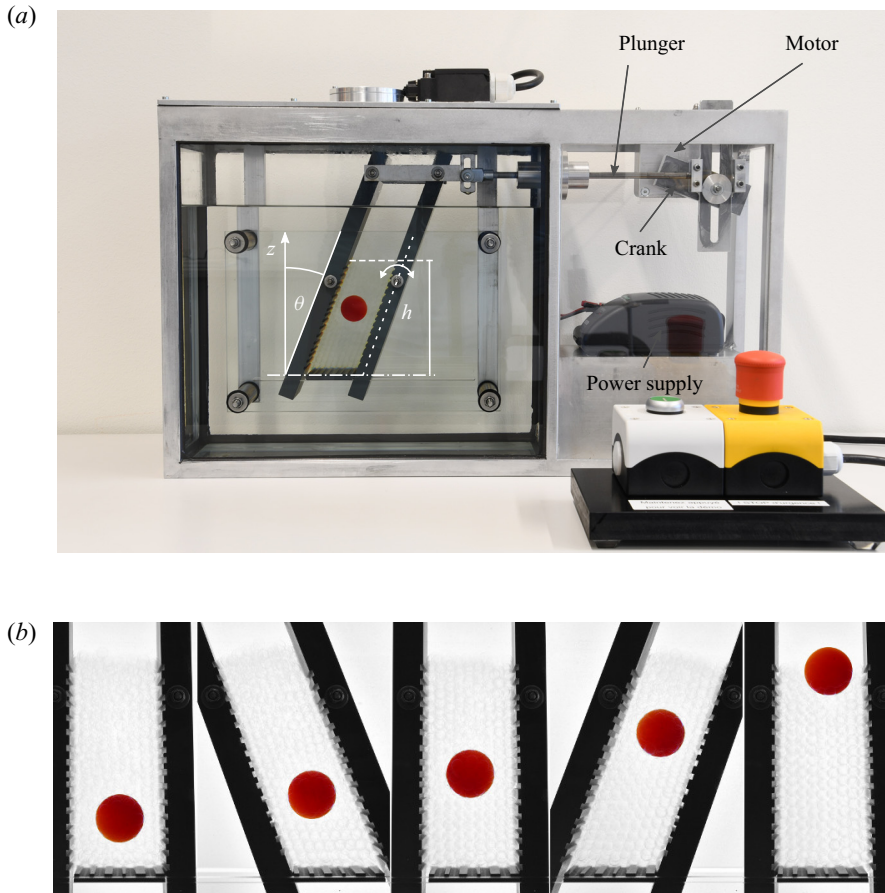


Figure 2. (a) A photograph of the experimental apparatus showing the power supply, motor, crank and plunger that drive the upper end of the pivoted parallel PVC plates from side to side. The two pivot points are located in the middle of the sidewalls and one of them is indicated on the photo. The base plate sits in a notched groove and is able to move freely from side to side in response to the driving motion. The volume between the pivoted PVC plates is filled with a granular material of thickness  $h$  that is composed of large and small borosilicate glass beads with diameters  $d_l$  and  $d_s$ , respectively. The whole system is submersed in a refractive index matched fluid, consisting of benzyl alcohol and ethanol, which makes the majority of particles transparent and allows the position of the semi-opaque red intruder to be easily identified. (b) An image sequence showing the rise of a large red intruder of diameter  $d_l = 25$  mm through a background medium of small particles of diameter  $d_s = 6$  mm over a number of oscillatory cycles. The small grains are just visible so it is possible to see the free surface. A supplementary movie available at <https://doi.org/10.1017/jfm.2021.227> showing the operation of experimental apparatus is available online.

Figure 2(b) and the first supplementary movie show how, over a series of cycles, the large red intruder is progressively squeezed upwards until it reaches the top of the cell. To analyse this motion it is useful to define a coordinate system  $Oxyz$  with the horizontal  $x$ -axis orientated in the direction of shear, the horizontal  $y$  axis across the cell and the  $z$  axis pointing vertically upwards. Assuming that the PVC plates are pivoted at a height  $z = z_{pivot}$  their imposed horizontal displacement field is

$$x = (z - z_{pivot}) \sin(\omega t) \tan \theta_{max}, \quad (3.1)$$

where  $\omega$  is the frequency and  $\theta_{max}$  is the maximum angle of displacement of the sidewalls measured from the vertical axis. Typically  $\theta_{max}$  ranges between  $22.5^\circ$  and  $25^\circ$  in the

### An experimental scaling law for particle-size segregation

experiments presented here. Assuming that the resulting velocity  $\mathbf{u}$  within the granular material is spatially uniform in each  $(x, y)$ -plane, the resulting velocity components are

$$u = (z - z_{pivot})\omega \cos(\omega t) \tan \theta_{max}, \quad v = 0, \quad w = 0, \quad (3.2)$$

respectively. The shear rate  $\dot{\gamma} = 2\|\mathbf{D}\|$  where  $\|\mathbf{D}\| = \sqrt{\frac{1}{2}\text{tr}(\mathbf{D}^2)}$  is the second invariant of the strain-rate tensor  $\mathbf{D} = (\nabla\mathbf{u} + (\nabla\mathbf{u})^T)/2$ . For the imposed bulk velocity field (3.2) it follows that the shear rate

$$\dot{\gamma} = \left| \frac{du}{dz} \right| = \omega |\cos(\omega t)| \tan \theta_{max}. \quad (3.3)$$

This varies in time, but is spatially uniform throughout the shear cell. The average shear rate over one complete cycle is

$$\dot{\gamma}_m = \frac{\omega}{2\pi} \int_0^{2\pi/\omega} \dot{\gamma} dt = \frac{2\omega}{\pi} \tan \theta_{max}. \quad (3.4)$$

The motor which drives the oscillatory shear cell has a variable voltage input, so the applied shear rate depends directly on the voltage and the amplitude of the crank connected to the plunger. Monodisperse experiments with four 6 mm opaque tracers in a 6 mm translucent media sheared at  $\dot{\gamma}_m = 1.1 \text{ s}^{-1}$  have been performed to check that the segregation is not caused by secondary convection in the underlying flow. A supplementary movie showing this is available online.

### 3.2. Refractive-index matching, image acquisition and particle tracking

The experiments rely on the refractive-index matching (RIM) technique to make the intruder visible. This is achieved by using transparent borosilicate glass beads for the background media and submerging them in a mixture of benzyl alcohol and ethanol. A summary of the material properties is given in table 1. A calibration procedure was required to get the right index match. An Atago RX 5000  $\alpha$  refractometer was therefore used to measure samples of the interstitial fluid. The initial mixture was based on the measurement tables of Chen, Lin & Tu (2012). Further adjustments to obtain the desired value of  $n_r = 1.4726$  were done by adding small quantities of either ethanol or benzyl alcohol. A value of  $n_r$  in between 1.471 and 1.472 were acceptable to clearly observe the intruder, a condition that improved for a period of time due to the faster evaporation of ethanol. For the same reason, values over 1.473 were undesirable despite an initially good match. The effect of the RIM is shown in figure 3(b) where a large red intruder can clearly be seen in the submersed lower two thirds of the image, but is completely obscured by the small particles in the dry upper third of the image.

The RIM technique allows the intruder to be clearly seen throughout the experiment (figure 2b). Image acquisition was performed with a Basler acA2000-165uc camera positioned in front of the shear box. Different frame rates were used for each experiment, but for most experiments recording was done at 10 frames per second. Particle identification was done using the `imfindcircles` routine implemented in Matlab. The single-intruder tracking was performed using the code of Crocker & Grier (1996). As well as tracking the opaque intruder this code also helped to identify, and exclude, false intruders, which could occur when the intruder size was close to that of the background medium (figure 3c). Figure 4 shows two space–time plots constructed by taking the vertical line of pixels through the centre of the intruder at each frame and plotting them adjacent to

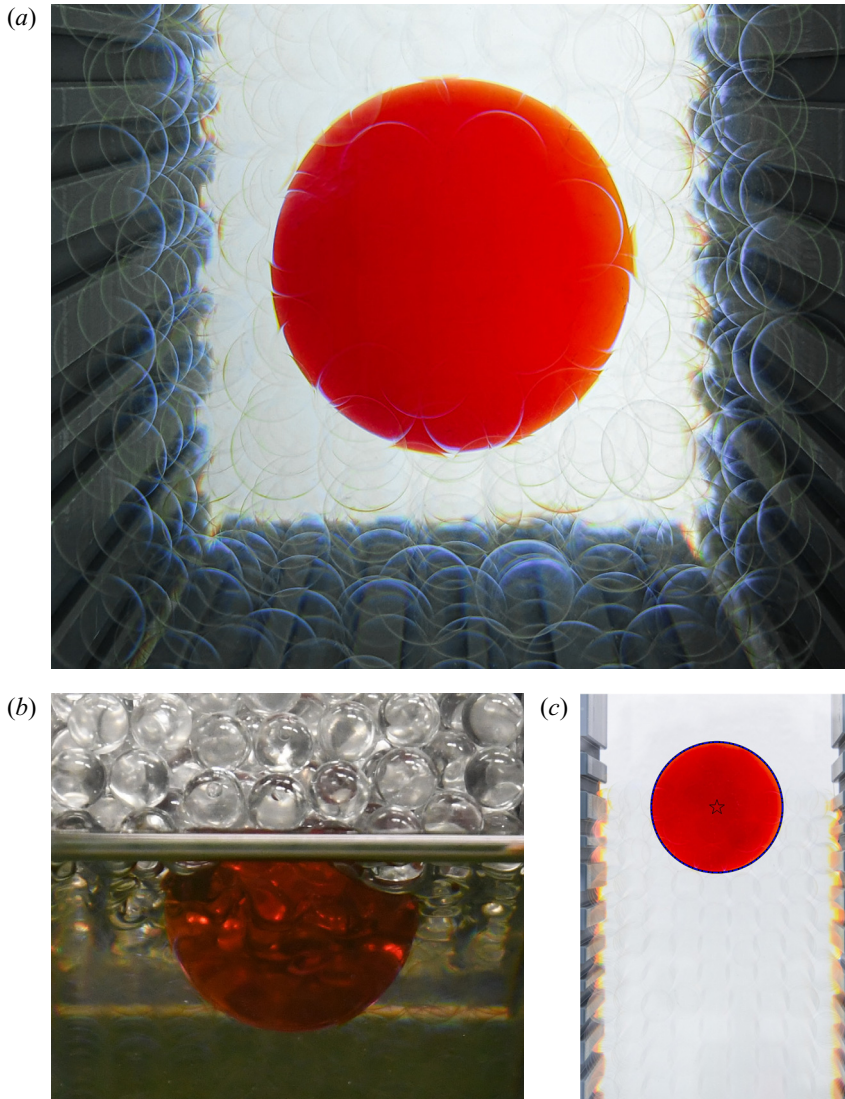


Figure 3. (a) Close-up photograph to show how the random profile structure of the pivoting and sliding walls helps to prevent the formation of crystalline structures in the particles surrounding the intruder. (b) Image showing the contrast between dry and wet conditions using the RIM technique with transparent borosilicate glass beads and a mixture of benzyl alcohol and ethanol. (c) Semi-opaque red intruder identified with the image analysis code.

Material	$n_r$	$\rho_*$ (g cm <sup>-3</sup> )	$\eta$ (cP)	Supplier
Borosilicate glass	1.4726	2.2	NA	Schäffer Glas
Benzyl alcohol	1.5396	1.044	5.474	Acros Organics
Ethanol	1.3656	0.789	1.2	Fisher Scientific

Table 1. Refractive indices  $n_r$ , intrinsic densities  $\rho_*$ , viscosities  $\eta$  and suppliers for the materials used in the refractive-index matched experiments.

## An experimental scaling law for particle-size segregation

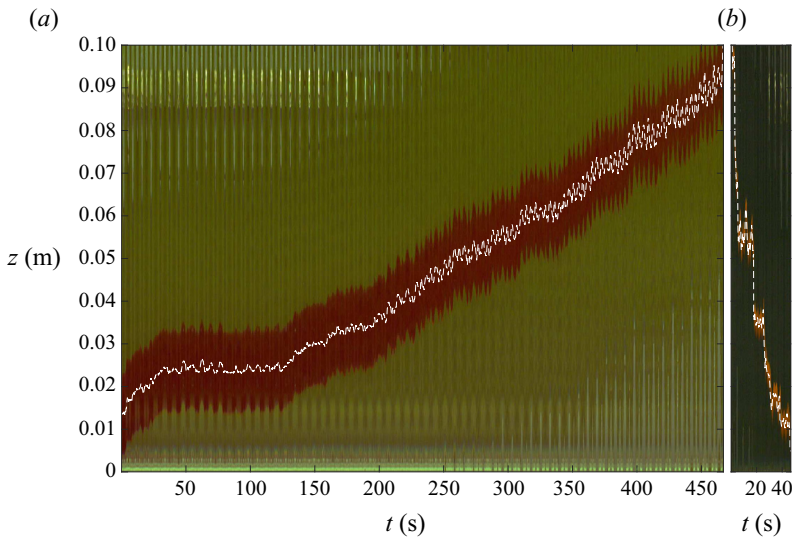


Figure 4. (a) Space–time plot of a large intruder of diameter  $d_l = 19$  mm segregating upwards in a medium of small particles of diameter  $d_s = 6$  mm subject to an average shear rate  $\dot{\gamma}_m = 0.26 \text{ s}^{-1}$  (taken from set 2 in table 2). The space–time plot is made by plotting the vertical line of pixels that passes through the centre of the large particle at each time. The intruder therefore appears as a band of red, while the index matched interstitial fluid and the background medium of small particles appear green. The trajectory of the centre of the large intruder as a function of time is shown with the white dashed line. (b) Space–time plot of small intruder particle of diameter  $d_s = 6$  mm percolating down through a matrix of large particles of diameter  $d_l = 14$  mm at a shear rate  $\dot{\gamma}_m = 0.34 \text{ s}^{-1}$  (taken from set 4 in table 2). In this experiment the background medium appears black while the intruder is orange. The intruder centre as a function of time is shown with a white dashed line.

one another. It is striking that for comparable size ratios and shear rates the large intruder takes much longer to be squeezed up to the free surface than the small intruder takes to percolate down to the base. It is also very significant that the trajectories of the intruder centres are both curved.

### 3.3. Experimental data sets

A series of five sets of experiments were performed in order to understand the functional dependence of the segregation velocity magnitude  $f_{sl}$ . Sets 1 and 2 correspond to experiments with a single large intruder rising through a medium of small particles. In set 1 the diameter of the large and small particles are held constant and the shear rate is varied, while in set 2 the diameter of the small particles and the shear rate are held constant and the diameter of the large intruder is changed. These sets represent experimental conditions where  $\phi = 1^-$ . Sets 3, 4 and 5 all relate to a small intruder segregating through a matrix of large grains, when  $\phi = 0^+$ . In sets 3 and 4 the shear rate is varied for two different small intruder diameters, while in set 5 the shear rate is held constant and the small intruder diameter is changed. The experimental conditions of all the sets are summarized in table 2.

## 4. Preliminary interpretation of the data

### 4.1. Dimensional analysis

The experimental data are complex and contain a number of functional dependencies that are hard to interpret without a clear initial hypothesis. It is therefore useful to consider what dimensional analysis can say about the functional behaviour of the segregation velocity

Set	Intruder	$d_l$ (mm)	$d_s$ (mm)	$R = d_l/d_s$	$\dot{\gamma}_m$ (s <sup>-1</sup> )
1	Large	19	6	3.17	0.26
		19	6	3.17	0.42
		19	6	3.17	0.59
		19	6	3.17	0.77
2	Large	10	6	1.67	0.26
		12	6	2	0.26
		19	6	3.17	0.26
		25	6	4.17	0.26
3	Small	14	8	1.75	0.34
		14	8	1.75	1.10
		14	8	1.75	2.30
4	Small	14	6	2.33	0.34
		14	6	2.33	0.63
		14	6	2.33	0.87
5	Small	14	12	1.17	0.34
		14	10	1.4	0.34
		14	8	1.75	0.34
		14	6	2.33	0.34
		14	4	3.5	0.34

Table 2. Diameters of the large particles  $d_l$ , small particles  $d_s$ , the size ratio  $R = d_l/d_s$  and average shear rates  $\dot{\gamma}_m$  for each experimental set 1–5. Sets 1–2 correspond to a single large intruder rising through a matrix of small particles, whereas sets 3–5 correspond to a single small particle percolating down through a matrix of large grains.

magnitude  $f_{sl}$  before presenting the results. For a dry bidisperse mixture of large and small particles,  $f_{sl}$  is considered to be an output of the system. The inputs are the particle sizes  $d_l$  and  $d_s$ , the intrinsic density of the grains  $\rho_*$ , the volume fraction of small particles  $\phi^s = 1 - \phi^l$  per unit granular volume, the solids volume fraction  $\Phi$ , the bulk shear stress  $\tau$ , the pressure  $p$ , gravity  $g$  and the shear rate  $\dot{\gamma}$ . This is a total of nine variables with three primary dimensions (mass, length and time), so dimensional analysis implies that there are six independent non-dimensional quantities

$$\mu = \frac{\tau}{p}, \quad I = \frac{\dot{\gamma}\bar{d}}{\sqrt{p/\rho_*}}, \quad \Phi, \quad P = \frac{p}{\rho_*g\bar{d}}, \quad R = \frac{d_l}{d_s}, \quad \phi^s, \quad (4.1a-f)$$

where  $\mu$  is the friction,  $I$  is the generalized inertial number in which  $\bar{d}$  is the volume fraction weighted average particle diameter

$$\bar{d} = \phi^l d_l + \phi^s d_s, \quad (4.2)$$

$P$  is the non-dimensional pressure and  $R = d_l/d_s$  is the grain-size ratio. In this analysis, the experimental system size and any higher gradients of the variables are implicitly assumed not to be of importance. For a monodisperse system in the absence of gravity, only the first three non-dimensional variables in (4.1a-f) are relevant, and (4.2) reduces to the monodisperse particle diameter. It was this type of dimensional analysis combined with observations from DPM simulations and experiments that led to the development of the incompressible  $\mu(I)$ -rheology (GDR-MiDi 2004; Jop *et al.* 2006), which has advanced our understanding of the rheology of monodisperse granular flows.

Dimensional analysis also provides a powerful way of interpreting the segregation experiments in this paper. It is assumed that it is the combination of shear-induced gravity

driven percolation (kinetic sieving) and squeeze expulsion (Middleton 1970; Bridgwater *et al.* 1985; Savage & Lun 1988; Gray & Thornton 2005; Gray 2018) that generate the dominant mechanism for segregation in dense granular flows. In particular, dimensional analysis implies that the segregation velocity magnitude should scale as

$$f_{sl} \sim \dot{\gamma} \bar{d} \mathcal{G}(\mu, I, \Phi, P, R, \phi^s), \quad (4.3)$$

where  $\dot{\gamma} \bar{d}$  is chosen as a reference scale and  $\mathcal{G}$  is an arbitrary function of the six non-dimensional variables defined in (4.1a–f). The five sets of experiments detailed in table 2 provide key observations that help to constrain the functional form of  $\mathcal{G}$ .

#### 4.2. Fundamental observations and resulting hypothesis

This paper makes four key assumptions based on the observations (a)–(d) below: (a) Experimental data sets 1, 3 and 4 imply that the segregation velocity magnitude  $f_{sl}$  scales linearly with the shear rate  $\dot{\gamma}$  for both large and small intruders. (b) Experimental set 2 implies that the rise velocity of large intruders scales linearly with the particle size ratio  $R$ , and since it necessarily shuts off when  $R = 1$ , this implies that  $f_{sl}$  scales linearly in  $R - 1$  in the limit  $\phi^s = 1^-$ . (c) Set 5 shows that in the limit  $\phi^s = 0^+$  small intruders exhibit an approximately quadratic dependence on  $R - 1$  for large size ratios, but have the same linear dependence on  $R - 1$ , as the large intruders, for small size ratios in the range  $[1, 1.5]$ . (d) All of the data sets in 1–5 show that the large and small intruders move along curved trajectories (see e.g. figure 4), with slower percolation and rise rates deeper in the flow, where the lithostatic pressure is higher. These trajectories are well approximated by quadratic curves. Since the pressure is lithostatic in the shear cell, this suggests that  $f_{sl}$  is proportional to  $1/(\mathcal{C} + P)$ , where the non-dimensional constant  $\mathcal{C}$  has been introduced to prevent a singularity when  $P = 0$  at the free surface.

The four key experimental observations (a–d) above suggest that the segregation velocity magnitude can be written as

$$f_{sl} = \mathcal{B} \dot{\gamma} \bar{d} \frac{\mathcal{F}(R, \phi^s)}{\mathcal{C} + P}, \quad (4.4)$$

where  $\mathcal{B}$  and  $\mathcal{C}$  are non-dimensional constants and  $\mathcal{F}$  is a function of  $R$  and  $\phi^s$ . The particle size-ratio dependence is encapsulated in  $\mathcal{F}$ , which satisfies the limits

$$\mathcal{F}(R, 1^-) = R - 1, \quad (4.5)$$

$$\mathcal{F}(R, 0^+) = R - 1 + \mathcal{E}(R - 1)^2, \quad (4.6)$$

where  $\mathcal{E}$  is another non-dimensional constant. A simple functional form that captures the single large and small intruder cases (4.5) and (4.6) is

$$\mathcal{F} = (R - 1) + \mathcal{E} \Lambda(\phi^s)(R - 1)^2, \quad (4.7)$$

where the function  $\Lambda$  satisfies the constraints

$$\Lambda(0) = 1, \quad \text{and} \quad \Lambda(1) = 0. \quad (4.8a,b)$$

A very simple linear function for  $\Lambda$  will be investigated further in § 7.

Substituting for the non-dimensional pressure  $P$  from the scaling (4.1a–f) the segregation velocity magnitude can be written as

$$f_{sl} = \mathcal{B} \frac{\rho_* g \dot{\gamma} \bar{d}^2}{\mathcal{C} \rho_* g \bar{d} + p} \mathcal{F}(R, \phi^s). \quad (4.9)$$

This formula captures the key processes of gravity, shear and pressure that drive kinetic sieving and squeeze expulsion during the segregation of particles of different sizes and

size ratios. The local small particle concentration  $\phi^s = 1 - \phi^l$  enters through the average grain size (4.2) and the nonlinear size-ratio dependence (4.7), and automatically generates asymmetry in the segregation flux functions. Equation (4.9) neglects any dependence on the friction of the particles  $\mu$  and the solids volume fraction  $\Phi$ . Such dependencies may exist (see Golick & Daniels 2009; Guillard *et al.* 2016; Jing *et al.* 2017), but they add an extra level of complexity that goes beyond the scope of this paper. Since  $I = \dot{\gamma}d/\sqrt{p/\rho_*}$  is linear in the shear rate  $\dot{\gamma}$ , (4.9) can be reformulated to have a linear inertial number dependence instead of a linear shear-rate dependence. Importantly the experimental observation (a), above, implies that there is either a linear shear-rate dependence or a linear inertial number dependence, but to leading order, at least, other shear rate or inertial number dependencies are not permitted.

#### 4.3. Effect of the interstitial fluid

Equations (4.4) and (4.9) take no account of the interstitial fluid present in the experiments in § 3. Thornton *et al.* (2006) used a three phase mixture theory, composed of large grains, small grains and an interstitial fluid, to show that the segregation velocity magnitude  $f_{sl}$  was moderated by the relative density difference

$$\hat{\rho} = \frac{\rho_* - \rho_*^f}{\rho_*}, \quad (4.10)$$

where  $\rho_*^f$  is the density of the fluid. If this multiplicative factor is included then  $f_{sl} = 0$  when  $\rho_*^f = \rho_*$ , and the particles do not segregate. This is consistent with the fluid density matched bidisperse experiment of Vallance & Savage (2000) in which no significant segregation was observed. Vallance & Savage (2000) also made the rather counterintuitive observation that the segregation was slightly weaker in water than in a water–ethanol mixture that was 3.7 times more viscous. The viscosity therefore does not suppress segregation as Vallance & Savage (2000) had hypothesized, but, instead, it is the relative density difference  $\hat{\rho}$  that explains their results (Thornton *et al.* 2006). All the experiments in this paper are performed with the same interstitial fluid, and for simplicity the factor  $\hat{\rho}$  is not explicitly included throughout most of the paper. However, in § 8 the dry DPM simulations of Thornton *et al.* (2012) are considered, and to compare the theory it is necessary to correct the experimentally measured value of  $\mathcal{B}$  to account for the absence of interstitial fluid.

#### 4.4. Intruder trajectories

In the shear box the gravitational acceleration vector  $\mathbf{g}$  points downwards parallel to the  $z$  axis, i.e.  $\mathbf{g} = -g\mathbf{k}$ , where  $\mathbf{k}$  is the unit vector in the  $z$ -direction. For the bulk velocity field defined in (3.2) it follows from (2.8) that, in the absence of diffusion, the vertical velocity of the large particles satisfies

$$w^l = \frac{dz^l}{dt} = f_{sl}\phi^s, \quad (4.11)$$

where  $f_{sl}$  is given by (4.9). For the case of a single large intruder,  $\phi^s = 1^-$ , and hence the average particle size  $\bar{d} = d_s$ . The large particle trajectory therefore satisfies the ordinary

differential equation (ODE)

$$\frac{dz^l}{dt} = \mathcal{B} \frac{\rho_* g \dot{\gamma} d_s^2}{C \rho_* g d_s + p} \mathcal{F}(R, 1^-). \quad (4.12)$$

Substituting for  $\mathcal{F}(R, 1^-)$  from (4.5) and assuming that the pressure in the grains is lithostatic

$$p = \rho_* g \Phi(h - z), \quad (4.13)$$

the ODE (4.12) reduces to

$$\frac{dz^l}{dt} = \mathcal{B} \frac{\dot{\gamma} d_s^2 (R - 1)}{C d_s + \Phi(h - z^l)}. \quad (4.14)$$

This is separable and can be integrated, subject to the initial condition that  $z^l = z_0^l$  at  $t = 0$ , to show that time is a quadratic function  $\mathcal{Z}^l$  of the vertical coordinate  $z^l$ , i.e.

$$\mathcal{K}^l t = C d_s (z^l - z_0^l) + \frac{\Phi}{2} [(h - z_0^l)^2 - (h - z^l)^2] = \mathcal{Z}^l(z^l), \quad (4.15)$$

where the constant

$$\mathcal{K}^l = \mathcal{B} \dot{\gamma} d_s^2 (R - 1), \quad (4.16)$$

is different for each individual experiment. Note that  $d_s$  and  $\Phi$ , which arise in the definition of  $\mathcal{Z}^l$  in (4.15), are the same for all the experiments in sets 1 and 2. The quadratic equation (4.15) can be solved to give an explicit formula for the trajectory of the large intruder

$$z^l = \frac{1}{\Phi} \left[ C d_s + \Phi h - \sqrt{C^2 d_s^2 + 2 C d_s \Phi (h - z_0^l) + \Phi^2 (h - z_0^l)^2 - 2 \Phi \mathcal{K}^l t} \right]. \quad (4.17)$$

An exactly analogous argument implies that at  $\phi^s = 0^+$  the trajectory of a small intruder satisfies the ODE

$$\frac{dz^s}{dt} = -\mathcal{B} \frac{\dot{\gamma} d_l^2 [(R - 1) + \mathcal{E}(R - 1)^2]}{C d_l + \Phi(h - z^s)}. \quad (4.18)$$

This is also separable and can be integrated, subject to the initial condition that  $z^s = z_0^s$  at  $t = 0$ , to show that time is a quadratic function  $\mathcal{Z}^s$  of the vertical coordinate  $z^s$ ,

$$\mathcal{K}^s t = -C d_l (z^s - z_0^s) - \frac{\Phi}{2} [(h - z_0^s)^2 - (h - z^s)^2] = \mathcal{Z}^s(z^s), \quad (4.19)$$

where the constant

$$\mathcal{K}^s = \mathcal{B} \dot{\gamma} d_l^2 [(R - 1) + \mathcal{E}(R - 1)^2], \quad (4.20)$$

changes between experiments. In all the experiments in sets 3–5 the values of  $d_l$  and  $\Phi$  in the definition of  $\mathcal{Z}^s$  are the same. The quadratic equation (4.19) can be solved to give an explicit formula for the small intruder trajectory

$$z^s = \frac{1}{\Phi} \left[ C d_l + \Phi h - \sqrt{C^2 d_l^2 + 2 C d_l \Phi (h - z_0^s) + \Phi^2 (h - z_0^s)^2 + 2 \Phi \mathcal{K}^s t} \right]. \quad (4.21)$$

A key test of this scaling argument and the fundamental assumptions (a)–(d) in § 4.2 is whether the intruder trajectories (4.17) and (4.21) are able to collapse all of the data with the same choices of the non-dimensional constants  $\mathcal{B}$ ,  $\mathcal{C}$  and  $\mathcal{E}$ .

#### 4.5. The role of particle diffusion

It is important to note that the intruder trajectories calculated in § 4.4 implicitly assume that there is no diffusion. In fact, experimental observations suggest that there is a significant amount of self-diffusion that leads to the intruders performing random walks around the mean path. Utter & Behringer (2004) used a two-dimensional Couette cell to make detailed experimental measurements of the self-diffusion in a monodisperse system of disks. They concluded that the diffusion was anisotropic, but that to leading order the diffusivity was proportional to  $\dot{\gamma}d^2$ , where  $d$  was the particle diameter. The natural generalization of this result to polydisperse systems is to replace the particle diameter with the mean particle diameter (4.2) to give

$$\mathcal{D}_{sl} = \mathcal{A}\dot{\gamma}\bar{d}^2, \quad (4.22)$$

where  $\mathcal{A}$  is a non-dimensional constant. Figure 9(b) in Utter & Behringer's (2004) paper shows that the tangential diffusivity implies  $\mathcal{A} = 0.223$ , whereas the radial diffusivity implies  $\mathcal{A} = 0.108$ . The simulations in § 7 adopt the lower value of  $\mathcal{A}$ , because it is based on measurements of the diffusivity made normal to the direction of shear, which is also the predominant direction for diffusion and segregation in the shear box experiments. Note, that since  $\bar{d} = d_s$  for a large intruder and  $\bar{d} = d_l$  for a small intruder equation (4.22) implies that there will be much more diffusion, and hence variability, for the small intruder paths than for the large intruders.

### 5. Large intruder experiments

The segregation of a single large intruder is stable and robust, especially when the size ratio is large. This is a reflection of the fact that, according to the diffusion scaling (4.22), the underlying self-diffusion within the small particle matrix is lower than for a large particle matrix. Larger size ratio intruders also have a lot of contacts with the surrounding small grains, which provides another mechanism for averaging the natural fluctuations. As a result the large intruders only occasionally migrate to the PVC side plates, where they can become stuck when the particle size ratio  $R$  is close to unity. To determine the values of  $\mathcal{B}$  and  $\mathcal{C}$  a global least squares fit is made to all the large intruder trajectories in experimental sets 1 and 2. This suggests that

$$\mathcal{B} = 0.3744, \quad \text{and} \quad \mathcal{C} = 0.2712. \quad (5.1a,b)$$

In practice, the constant  $\mathcal{C}$  only changes the gradient of the trajectory close to the free surface, and this is least well constrained because the experimental free surface is not clearly defined at the particle scale. Good fits to the data can also be obtained by assuming  $\mathcal{C} = 0$ , in which case  $\mathcal{B} = 0.3615$ . This is only a 3.45% difference. Setting  $\mathcal{C} = 0$  does, however, introduce a pressure singularity at  $p = 0$ , which implies that the segregation velocity becomes infinite at the free surface. This singularity is not only unphysical, but causes difficulties in numerical methods, so in the sections that follow  $\mathcal{C}$  is assumed to take its global value defined in (5.1a,b).

#### 5.1. Variable shear rate for the large intruders

The experimentally measured position of a large 19 mm intruder in a matrix of small 6 mm particles as a function of time is shown in figure 5, for four different shear rates. These experiments correspond to set 1 in table 2. The intruder struggles to segregate upwards when it is close to the bottom of the cell, but once it moves past a few layers it segregates faster and faster towards the surface. As a result the intruder trajectories all

An experimental scaling law for particle-size segregation

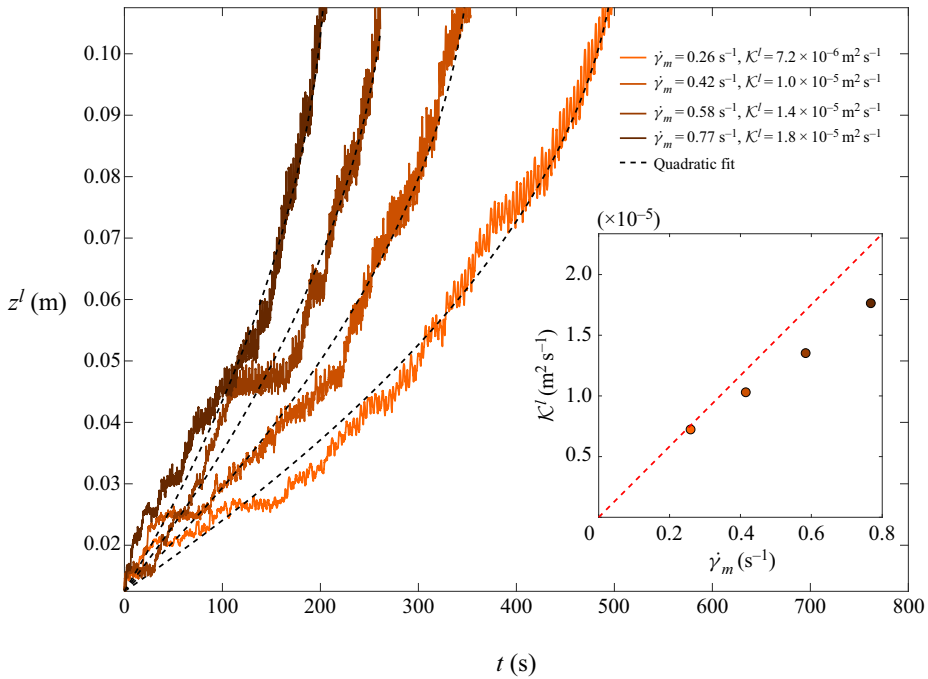


Figure 5. Experimentally measured position of a 19 mm large intruder segregating through a 6 mm matrix of small particles as a function of time, for four different imposed shear rates  $\dot{\gamma}_m = 0.26, 0.42, 0.59$  and  $0.77 \text{ s}^{-1}$ . Darker red lines correspond to higher shear rates. These data correspond to set 1 in table 2. For each case, (4.15) is fitted to the experimental data to determine the constant  $\mathcal{K}^l$  assuming that the depth  $h = 12 \text{ cm}$  and  $C = 0.2712$  is given by the global best fit to all the large intruder data. The fitted intruder trajectory in time (4.17) is then plotted for each  $\dot{\gamma}_m$  with dashed lines for comparison. The coefficient of determination ranges between 0.96 and 0.97 for the proposed fits. The inset shows the fitting constants  $\mathcal{K}^l$  as a function of  $\dot{\gamma}_m$ . These points are closely approximated by the global best fit straight (red dashed) line that passes through the origin (5.2), implying that  $f_{sl}$  has a linear shear-rate dependence.

show a pronounced curvature in time that are well fitted by the quadratic curves derived in § 4.4 using the global value of  $C$  defined in (5.1a,b). For each individual trajectory, (4.15) is fitted to the experimental data by determining the constant  $\mathcal{K}^l$  that gives the best approximation. Typically the fits were extremely good, with a coefficient of determination lying in the range 0.96–0.97. As the shear-rate  $\dot{\gamma}_m$  is increased the large intruder segregates to the surface faster and therefore the time to reach the surface decreases, while the fitting constant increases. The four values of  $\mathcal{K}^l$  are plotted as a function of  $\dot{\gamma}_m$  in the inset plot in figure 5, together with the theoretical straight line passing through the origin defined in (4.16), i.e.

$$\mathcal{K}^l = \mathcal{B}\dot{\gamma}_m d_s^2 (R - 1), \quad (5.2)$$

where it is assumed that  $\dot{\gamma} = \dot{\gamma}_m$  and  $\mathcal{B}$  is given by the global value in (5.1a,b). The points all lie close to the straight line, although for this subset of data the global fit is not quite the best fit. The data are, however, close to the global fit and is consistent with the fundamental assumption (a) in § 4.2 that the segregation velocity magnitude is linear in the shear rate.

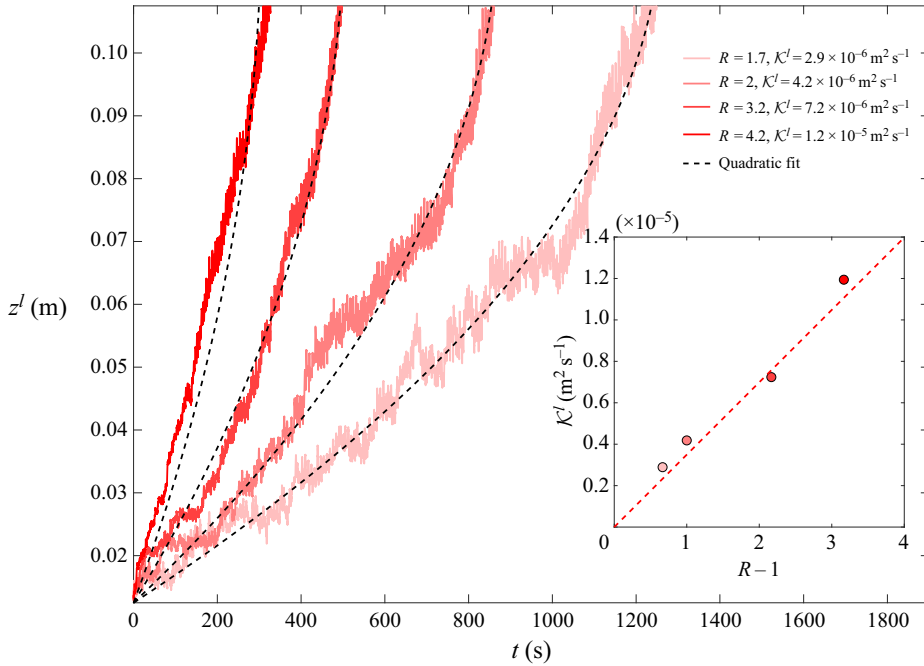


Figure 6. Experimentally measured position of a large intruder of size  $d_l = 10, 12, 19$  and  $25$  mm (darker red lines correspond to larger intruders) in a matrix of  $6$  mm small particles as a function of time, and at the same imposed shear rate  $\dot{\gamma}_m = 0.26 \text{ s}^{-1}$ . This corresponds to set 2 in table 2. For each case, (4.15) is fitted to the experimental data to determine the constant  $\mathcal{K}^l$  assuming that the depth  $h = 12$  cm and  $C = 0.2712$  is given by the global best fit to all the large intruder data. The fitted intruder trajectory in time (4.17) is then plotted for each size ratio  $R$  with dashed lines for comparison. The coefficient of determination ranges between 0.93 and 0.98. The inset shows the measured constants  $\mathcal{K}^l$  as a function of  $R - 1$ . These points are well approximated by a global best fit straight (red dashed) line that passes through the origin (5.2), implying that  $f_{sl}$  has a linear dependence on  $R - 1$ .

### 5.2. Variable size ratio for the large intruders

Figure 6 shows experimental set 2 (from table 2) in which both the shear rate  $\dot{\gamma}_m = 0.26 \text{ s}^{-1}$  and the small particle diameter  $d_s = 6$  mm are held constant, while the diameter of the large intruder  $d_l$  is varied. In this limit the average particle size  $\bar{d} = d_s$ , but the size ratio  $R$  changes between experiments. As the size ratio is increased the particles segregate faster and the time for a particle to rise from the bottom to the top of the cell decreases. In each case the large intruders describe curved trajectories in time as they rise through the cell. This implies that near the bottom of the cell the segregation rate is considerably lower than close to the surface, where the intruder moves notably faster. The intruder trajectories are all well approximated by the quadratic curves derived in § 4.4, although there is some evidence that the curves become more linear at high size ratios. The curves are fitted using a similar procedure to § 5.1, i.e. by determining the best value of the constant  $\mathcal{K}^l$  for each experiment using the global value of  $C$  defined in (5.1a,b). The fitted values of  $\mathcal{K}^l$  are plotted as a function of the size ratio  $R - 1$  in the inset of figure 6. The points lie extremely close to the theoretical straight line (5.2) that passes through the origin, indicating that the segregation rate magnitude  $f_{sl}$  is linear in  $R - 1$  even at high size ratios, as assumed in hypothesis (b) in § 4.2.

### 5.3. Collapse of all the large intruder experiments

All the large intruder trajectory data from sets 1 and 2 can be collapsed by plotting the quadratic function of the height  $\mathcal{Z}^l$ , defined in (4.15), as a function of scaled time  $\mathcal{B}\dot{\gamma}_m d_s^2 (R - 1)t$  as shown in figure 7. This collapse is based on (4.15) and (5.2), which imply that

$$\mathcal{Z}^l = \mathcal{B}\dot{\gamma}_m d_s^2 (R - 1)t. \quad (5.3)$$

The mapped trajectories should therefore all lie on the 45 degree line shown in figure 7. All the trajectories follow the right trend, but move slightly off the ideal straight line as they rise up through the cell. Some variability is to be expected because the theoretical large intruder trajectory completely ignores the effect of diffusion, which will generate random walks around the average behaviour captured by the theory. Some of the variability is also likely to be an artifact of the oscillatory shear cell, which moves through a maximum angle  $\theta_{max}$  before reversing direction, rather than shearing in a consistent direction. This reduces the particle rearrangements, somewhat, and creates brief interludes during which the large intruder oscillates around a given level, before rising upwards again. As can be seen in figure 7 these interludes create a horizontal offset in some of the shear-rate data, before the overall rise continues along a line parallel to the 45 degree line. The inset image in figure 7 shows the values of  $\mathcal{K}^l$  as a function of  $\dot{\gamma}_m d_s^2 (R - 1)$ . All the experimental points for variable shear rate and variable size ratio lie close to the theoretical straight line implied by the global fit with the values of  $\mathcal{B}$  and  $\mathcal{C}$  from (5.1a,b). This confirms that hypotheses (a), (b) and (d), made in § 4.2, are able to collapse all the large intruder data, with the same constant values of  $\mathcal{B}$  and  $\mathcal{C}$ .

## 6. Small intruder experiments

The small intruders typically percolate downwards much faster than the large particles segregate upwards (as shown in figure 4). It is also anticipated that the small intruders will be subject to much more diffusion than the large intruders, because the average grain size of the background medium  $\bar{d} = d_l > d_s$  in the diffusivity (4.22). These combined effects result in the small intruders segregating much more erratically than the large intruders. Several experimental difficulties were observed. The intruder could migrate towards the PVC side plates and become stuck, or get stuck on top of a layer of well-packed large particles. Experimental data where the intruder suddenly dropped down after being stuck for a large number of cycles were not considered to be representative. To ensure consistent data were collected, the experiments were repeated four times for  $R = 1.167$ , up to eight times for  $1.167 < R < 3.5$  and six times for  $R = 3.5$ . Three representative experimental curves were then selected, on the basis that the intruder did not contact the walls, and the segregation times were similar.

### 6.1. Variable shear rate for the small intruders

Figure 8 shows the trajectories of an 8 mm small intruder in a matrix of 14 mm large particles for three different shear rates corresponding to set 3 in table 2. The three representative profiles are plotted for each shear rate. The theoretical small particle trajectory is fitted to each curve using the same value of  $\mathcal{C}$  as in (5.1a,b), and the average value of  $\mathcal{K}^s$  is then used to determine the overall fit. There is quite a lot of variability about the individual fits, as anticipated, but the fitted trajectory captures the overall behaviour of the small intruders as they percolate downwards. As the shear rate is increased the time taken for intruder to reach the bottom of the cell decreases and  $\mathcal{K}^s$  increases. The values

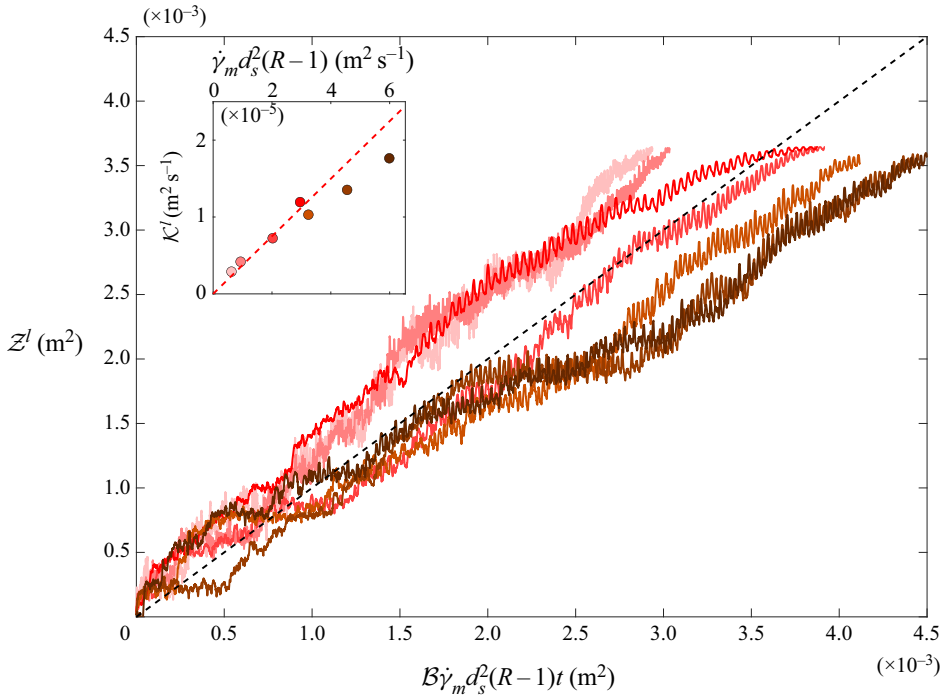


Figure 7. The large intruder trajectories for varying shear rate  $\dot{\gamma}_m$  and size ratio  $R$  are collapsed onto an approximately straight (dashed) 45 degree line by plotting the transformed height  $Z^l$ , defined in (4.15), against the scaled time  $B\dot{\gamma}_m d_s^2 (R - 1)t$ . The data correspond to all the cases in sets 1 and 2 in table 2. The inset plot shows the best fit values of the constants  $K^l$  for each of the experiments as a function of  $\dot{\gamma}_m d_s^2 (R - 1)$ . The red dashed line in the inset has gradient  $B = 0.3744$ , i.e. the global best fit value of  $B$ . The colours of the points and the lines are the same as those used in figures 5 and 6, where the legends are defined.

of  $K^s$  are plotted in the inset graph in figure 8 and show a clear linear dependence on the average shear rate  $\dot{\gamma}_m$ , consistent with the theoretical line

$$K^s = B\dot{\gamma}_m d_l^2 [(R - 1) + \mathcal{E}(R - 1)^2], \tag{6.1}$$

implied by (4.20). The quadratic dependence on  $R - 1$  in (6.1) suggests that the segregation rate could be much larger for higher size ratios. To test this, and to test that there is still a linear shear-rate dependence, figure 9 shows how a 6 mm small intruder percolates down through a matrix of 14 mm large particles at various shear rates. This corresponds to a size ratio  $R = 2.333$ , which is not that much larger than  $R = 1.75$  for the previous experiments in figure 8, but the time taken to reach the bottom of the cell for  $\dot{\gamma}_m = 0.34 \text{ s}^{-1}$  is approximately a quarter of that when the size ratio was  $R = 1.75$ . Importantly, however, the fitted values of  $K^s$  still exhibit a linear dependence on  $\dot{\gamma}_m$  as shown in the inset of figure 9. This observation suggests that the dramatic enhancement in the segregation rate of the small intruders at large size ratios, can be modelled through an additional quadratic size-ratio dependence in the function  $\mathcal{F} = \mathcal{F}(R, \phi^s)$  defined in (4.7) at low small particle volume fractions.

### 6.2. Variable size ratio for the small intruders

In order to determine the non-dimensional constant  $\mathcal{E}$  in (6.1) a series of experiments were performed at the same shear rate, but with variable size ratio. These correspond to

An experimental scaling law for particle-size segregation

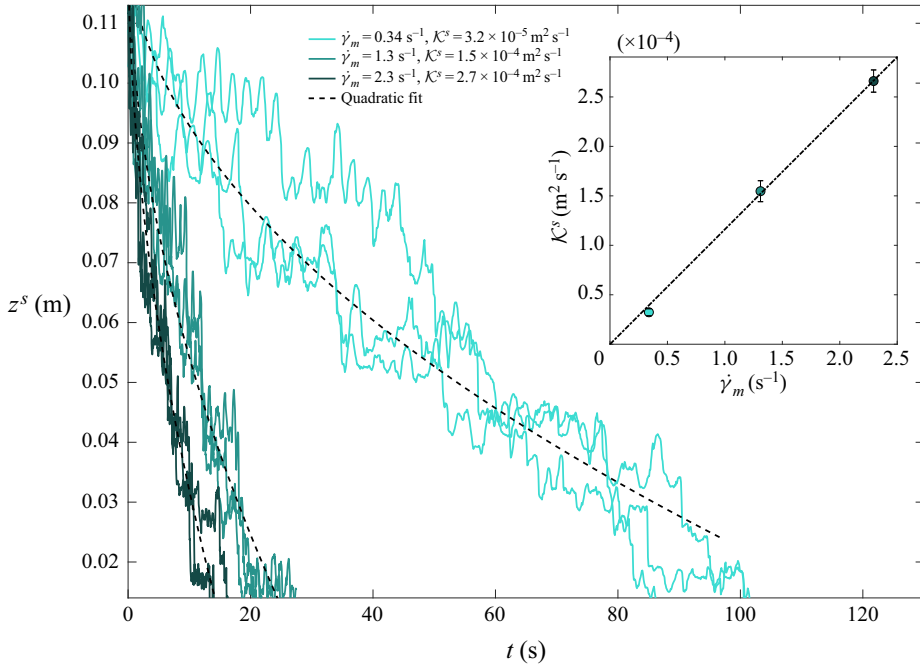


Figure 8. Measured position of a 8 mm small intruder segregating through a 14 mm matrix of large particles as a function of time for three different imposed shear rates  $\dot{\gamma}_m$  (darker turquoise lines correspond to higher shear-rates). Three representative experimental profiles are plotted for each experiment. These data correspond to set 3 in table 2. For each case, (4.19) is fitted to the data set and the value is then averaged over the three realizations to determine  $\mathcal{K}^s$ , assuming the same value of  $\mathcal{C}$  as in (5.1a,b). The average fitted intruder trajectory (4.21) is then plotted as a function of time for each  $\dot{\gamma}_m$  with dashed lines for comparison. The insets show the fitting constant  $\mathcal{K}^s$  as a function of  $\dot{\gamma}_m$ . All the points are closely approximated by a straight (dot-dashed) line that passes through the origin, implying that  $f_{SI}$  has a linear shear-rate dependence at moderate size ratios.

set 5 in table 2 and are shown in figure 10. Fits to the three sets of data shown for each case were performed in the same way as in § 6.1 and the values of  $\mathcal{K}^s$  are shown in the inset of figure 10. For size ratios close to unity the values of  $\mathcal{K}^s$  lie very close to the red dashed line, corresponding to (6.1) with  $\mathcal{E} = 0$ , using the same coefficients  $\mathcal{B}$  and  $\mathcal{C}$  that were determined for the large intruders in (5.1a,b). However, as the size ratio increases above  $R = 1.5$  the values of  $\mathcal{K}^s$  depart markedly from this line. The additional quadratic dependence on  $R - 1$  in (6.1) is, however, able to capture the dramatic increase in the segregation velocity at large size ratios. A least squares fit to the data suggests that

$$\mathcal{E} = 2.0957. \tag{6.2}$$

The small intruders therefore segregate with a linear  $R - 1$  dependence for size ratios close to unity, but segregate with an  $(R - 1)^2$  dependence at larger size ratios. This is consistent with the notion that small intruders find it increasingly easy to find holes in which to percolate, as the size ratio increases towards the limit of spontaneous percolation at  $R \simeq 6$ . Above this threshold, spontaneous percolation implies that small particles can percolate through a matrix of large grains even in the absence of shear (Bridgwater & Ingram 1971; Wilkinson & Edwards 1982), so this observation makes physical sense. The result is also backed up by recent DPM simulations of segregation at low small particle concentrations. To see this, compare the inset in figure 10 with figure 6(b) of Chassagne *et al.* (2020),

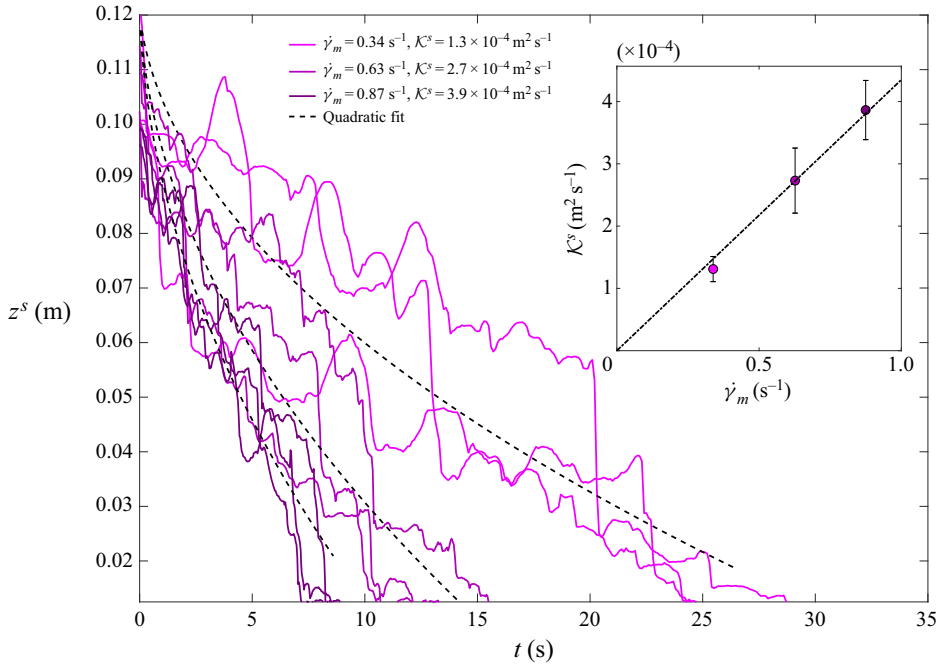


Figure 9. Measured position of a 6 mm small intruder segregating through a 14 mm matrix of large particles as a function of time for three different imposed shear rates  $\dot{\gamma}_m$  (darker magenta lines correspond to higher shear-rates). Three representative experimental profiles are plotted for each experiment. These data correspond to set 4 in table 2. For each case, (4.19) is fitted to the data set and the value is then averaged over the three realizations to determine  $\mathcal{K}^s$ , assuming the same value of  $\mathcal{C}$  as in (5.1a,b). The average fitted intruder trajectory (4.21) is then plotted as a function of time for each  $\dot{\gamma}_m$  with dashed lines for comparison. The insets show the fitting constant  $\mathcal{K}^s$  as a function of  $\dot{\gamma}_m$ . All the points are closely approximated by a straight (dot-dashed) line that passes through the origin, implying that  $f_{sl}$  has a linear shear-rate dependence even at larger size ratios.

which also shows a linear increase in the segregation rate for  $R$  close to unity and a nonlinear increase at larger grain-size ratios.

### 6.3. Collapse of all the small intruder experiments

All the small intruder data from sets 3, 4 and 5 in table 2 and shown in figures 8–10 can now be collapsed onto a single curve using the same coefficients  $\mathcal{B}$ ,  $\mathcal{C}$  and  $\mathcal{E}$ . This is achieved by plotting the quadratic function of the height  $\mathcal{Z}^s$  defined in (4.19) as a function of the scaled time  $\mathcal{B}\dot{\gamma}_m d_l^2 [(R-1) + \mathcal{E}(R-1)^2]t$  as shown in figure 11. This collapse is based on (4.19) and (4.20), which imply that

$$\mathcal{Z}^s = \mathcal{B}\dot{\gamma}_m d_l^2 [(R-1) + \mathcal{E}(R-1)^2]t. \quad (6.3)$$

The mapped trajectories should therefore lie on the 45 degree line in figure 11. The collapse for the individual trajectories is far from perfect for the reasons discussed at the beginning of § 6, which is to be anticipated, but they do follow the right general trend for a wide range of shear rates and particle size ratios. The collapse is much more convincing when the individual fitted values of  $\mathcal{K}^s$  are plotted against the theoretical line implied by (6.1), which is shown in the inset of figure 11. All the measured points lie very close to the theoretical straight line passing through the origin. This confirms that the small intruder data can be collapsed using the same values of the non-dimensional constants  $\mathcal{B}$ ,  $\mathcal{C}$  and  $\mathcal{E}$ .

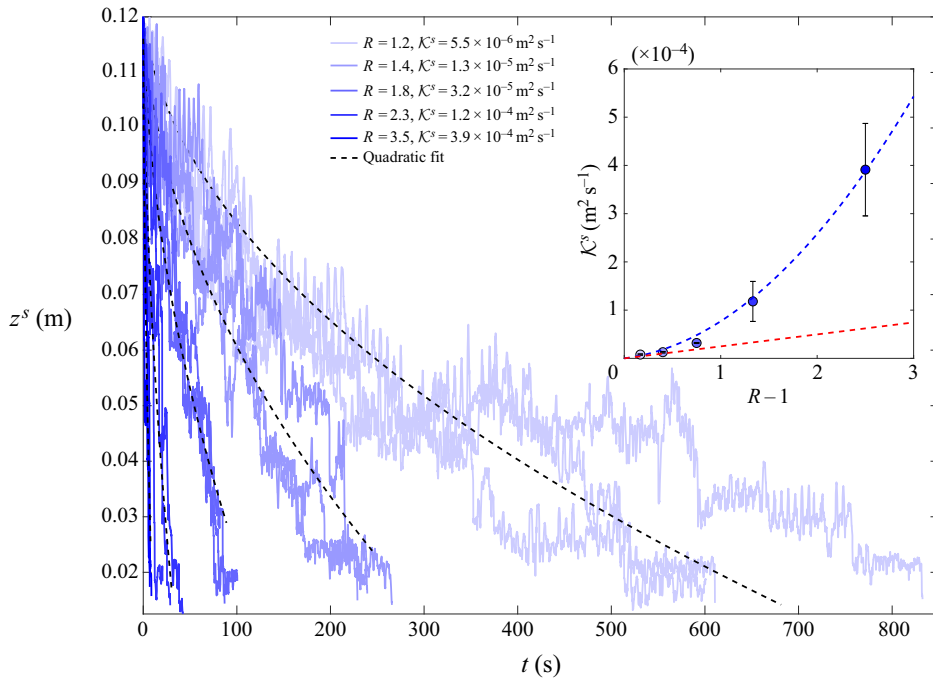


Figure 10. Experimentally measured position of a small intruder of size  $d_l = 12, 10, 8, 6$  and  $4$  mm in a matrix of  $14$  mm large particles as a function of time, and at the same imposed shear-rate  $\dot{\gamma}_m = 0.34 \text{ s}^{-1}$ . Three representative experimental profiles are plotted for each experiment. This corresponds to set 5 in table 2. For each case, (4.19) is fitted to the data set and the value is then averaged over the three realizations to determine  $K^s$ , assuming the same value of  $C$  as in (5.1a,b). The average fitted intruder trajectory (4.21) is then plotted as a function of time for each size ratio  $R$  with dashed lines for comparison. The inset shows the fitting constants  $K^s$  as a function of  $R - 1$ . At size ratios close to unity the constants follow the same linear dependence on  $R - 1$  as the large grains (red dashed line), but for larger size ratios the constants  $K^s$  become much larger. This is well fitted by the quadratic size-ratio dependence in (6.1) with  $\mathcal{E} = 2.0957$  (dashed blue line).

Moreover, the constants  $\mathcal{B}$  and  $\mathcal{C}$  are exactly the same as the values used to collapse the large intruder data in § 5. These results therefore validate our preliminary hypotheses (a)–(d) made in § 4.2.

## 7. Simulation of van der Vaart *et al.*'s (2015) experiment

The fully index matched experiment of van der Vaart *et al.* (2015), which was performed in a similar shear cell to that in this paper, provides an important constraint on the functional form of  $\mathcal{F}$ , since the volume fraction of small particles evolves through the complete range of  $\phi^s \in [0, 1]$ .

### 7.1. Summary of the equations and coefficients

In order to derive the governing equations, the particle-size distribution is assumed to be spatially uniform in the  $x$  and  $y$  directions. Substituting the gravity vector  $\mathbf{g} = -g\mathbf{k}$  and the velocity field (3.2) into (2.3) implies that the small particle segregation equation reduces to

$$\frac{\partial \phi^s}{\partial t} - \frac{\partial}{\partial z} (f_{sl} \phi^s \phi^l) = \frac{\partial}{\partial z} \left( \mathcal{D}_{sl} \frac{\partial \phi^s}{\partial z} \right), \quad (7.1)$$

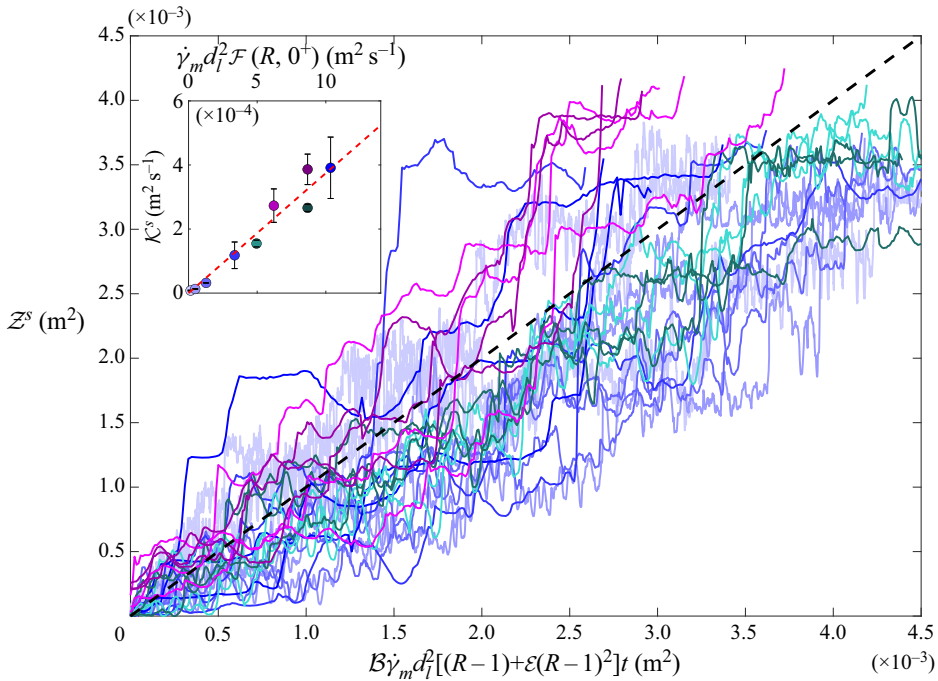


Figure 11. The small intruder trajectories for varying shear rate  $\dot{\gamma}_m$  and size ratio  $R$  are collapsed onto an approximately straight (dashed) 45 degree line by plotting the transformed height  $\mathcal{Z}^s$ , defined in (4.19), against the scaled time  $\mathcal{B}\dot{\gamma}_m d_l^2 [(R - 1) + \mathcal{E}(R - 1)^2]t$ . The data correspond to all the cases in sets 3, 4 and 5 in table 2. The inset plot shows the best fit values of the constants  $\mathcal{K}^s$  for each of the experiments as a function of  $\dot{\gamma}_m d_l^2 \mathcal{F}(R, 0^+)$ . The red dashed line in the inset has gradient  $\mathcal{B} = 0.3744$ , i.e. the global best fit value of  $\mathcal{B}$ . The colours of the points and the lines are the same as those used in figures 8–10, where the legends are defined.

where  $f_{sl}$  and  $\mathcal{D}_{sl}$  are the segregation velocity magnitude and diffusivity, respectively. Substituting the lithostatic pressure (4.13) into (4.9) and cancelling  $\rho_*g$ , implies that

$$f_{sl} = \frac{\mathcal{B}\dot{\gamma}\bar{d}^2\mathcal{F}}{\mathcal{C}\bar{d} + \Phi(h - z)}, \tag{7.2}$$

where the size-ratio dependence is encapsulated in

$$\mathcal{F} = (R - 1) + \mathcal{E}\Lambda(\phi^s)(R - 1)^2. \tag{7.3}$$

The function  $\Lambda = \Lambda(\phi^s)$  satisfies the constraints that  $\Lambda(0) = 1$  and  $\Lambda(1) = 0$ . It describes the effect of the size ratio at intermediate concentrations, and allows  $\mathcal{F}$  to smoothly transition from the linear  $R - 1$  dependence of a large intruder (4.5) to the  $(R - 1)^2$  dependence (4.6) for a small intruder. The simplest possible form for  $\Lambda$  is the linear law

$$\Lambda = \phi^l = 1 - \phi^s, \tag{7.4}$$

which will be investigated here. However, much more complicated functions are possible, so long as they satisfy the constraints (4.8a,b). As discussed in §4.5 the diffusivity is assumed to take the form

$$\mathcal{D}_{sl} = \mathcal{A}\dot{\gamma}\bar{d}^2, \tag{7.5}$$

where the non-dimensional coefficient  $\mathcal{A}$  is determined by the experiments of Utter & Behringer (2004). The other non-dimensional coefficients  $\mathcal{B}$ ,  $\mathcal{C}$  and  $\mathcal{E}$  have been

$$\mathcal{A} = 0.108, \quad \mathcal{B} = 0.3744, \quad \mathcal{C} = 0.2712, \quad \mathcal{E} = 2.0957$$

Table 3. Non-dimensional coefficients  $\mathcal{B}$ ,  $\mathcal{C}$ ,  $\mathcal{E}$  determined from the refractive-index matched shear-cell experiments. Note that it is anticipated that in the absence of an interstitial fluid the segregation rate will be enhanced (see § 4.3), which increases the assumed value of  $\mathcal{B}$ . The non-dimensional coefficient  $\mathcal{A}$  is taken from figure 9 of Utter & Behringer (2004).

determined by the shear box experiments in this paper and all of them are summarized in table 3.

### 7.2. Non-dimensionalization and numerical method

In order to solve the system of (7.1)–(7.5) it is useful to non-dimensionalize the equations using the same scalings as in van der Vaart *et al.* (2015), i.e.

$$t = T\tilde{t}, \quad z = h\tilde{z}, \quad (7.6a,b)$$

where  $T = 13$  s is the period of one cycle and  $h = 0.087$  m is the depth of the cell. It follows that the segregation equation (7.1) can be written in the non-dimensional form

$$\frac{\partial \phi^s}{\partial \tilde{t}} - \frac{\partial}{\partial \tilde{z}} (S_r \phi^s \phi^l) = \frac{\partial}{\partial \tilde{z}} \left( D_r \frac{\partial \phi^s}{\partial \tilde{z}} \right), \quad (7.7)$$

where the non-dimensional segregation rate and non-dimensional diffusivity are

$$S_r = \frac{Tf_{sl}}{h} = \frac{\mathcal{B}\dot{\gamma}T(\bar{d}/h)^2\mathcal{F}}{\mathcal{C}(\bar{d}/h) + \Phi(1 - \tilde{z})}, \quad (7.8)$$

$$D_r = \frac{T\mathcal{D}_{sl}}{h^2} = \mathcal{A}\dot{\gamma}T(\bar{d}/h)^2, \quad (7.9)$$

respectively. The period equals  $T = 2\pi/\omega$  by definition. It therefore follows from (3.4) that the average shear rate  $\dot{\gamma}_m$  times the period

$$\dot{\gamma}_m T = 4 \tan \theta_{max}, \quad (7.10)$$

where  $\theta_{max} = 30^\circ$  in the experiments of van der Vaart *et al.* (2015). The mean value  $\dot{\gamma}_m T$  is used to approximate  $\dot{\gamma}T$  in (7.8) and (7.9). The non-dimensional segregation equation (7.7) is solved subject to no flux conditions at the surface and the base of the cell

$$S_r \phi^s \phi^l + D_r \frac{\partial \phi^s}{\partial \tilde{z}} = 0, \quad \text{at } \tilde{z} = 0, 1, \quad (7.11)$$

and the initial condition

$$\phi^s = \begin{cases} 1, & \tilde{z} > 0.5, \\ 0, & \tilde{z} \leq 0.5, \end{cases} \quad (7.12)$$

so that all the small grains are above the large particles at the start of the experiment (van der Vaart *et al.* 2015). A Galerkin finite element solver (Skeel & Berzins 1990) is used to generate the results. This method is conveniently coded in the pdepe routine in Matlab and has been extensively tested in previous papers (Gray & Ancy 2011; Wiederseiner *et al.* 2011; Gray & Ancy 2015; van der Vaart *et al.* 2015). It should be noted, however, that this method fails when  $\mathcal{C} = 0$ , because in this case the segregation rate becomes unbounded at the free surface.

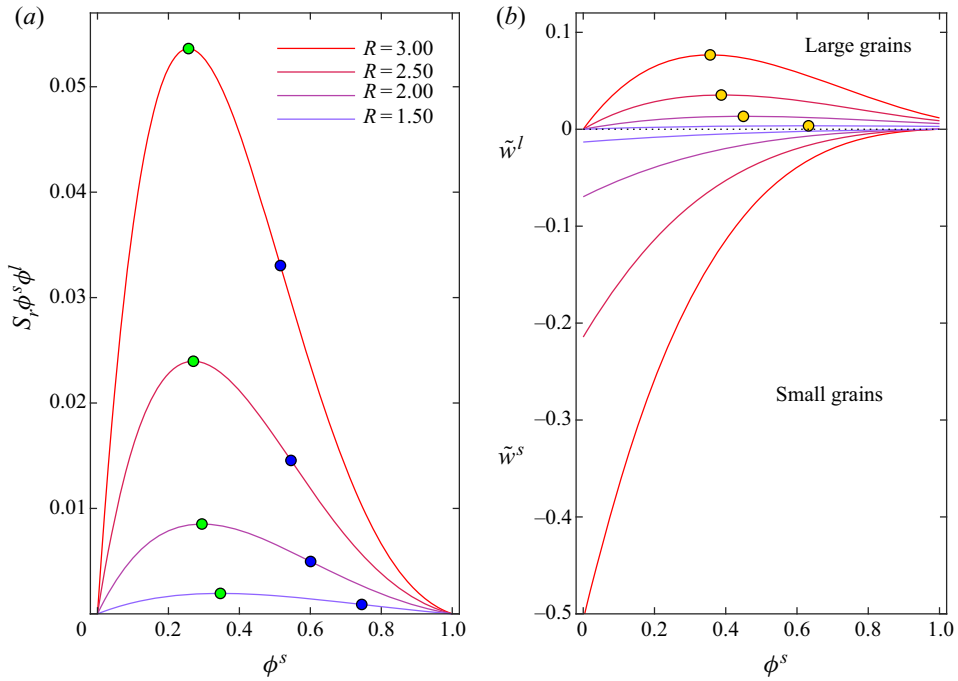


Figure 12. (a) The non-dimensional segregation flux  $S_r \phi^s \phi^l$  as a function of the small particle concentration  $\phi^s$ , for a range of grain-size ratios  $R = 1.5, 2, 2.5$  and  $3$ . The flux is evaluated with  $h = 87$  mm,  $T = 13$  s,  $\theta_{max} = 30^\circ$ ,  $d_s = 4$  mm and  $\hat{z} = 1/2$ , using the non-dimensional coefficients summarized in table 3. The green markers show the position of the maximum and the blue markers show the inflection point. (b) Shows the corresponding non-dimensional large and small particle segregation velocities,  $\tilde{w}^l$  and  $\tilde{w}^s$ , as a function of  $\phi$ . The yellow markers show the position of the maximum large particle segregation velocity, which occurs at intermediate concentrations.

### 7.3. Asymmetric segregation flux functions

It is interesting to see what the consequences the empirically derived scaling law has for the shape of segregation flux function. The non-dimensional segregation equation (7.7) implies that the non-dimensional segregation flux of large and small particles in the vertical direction are

$$\tilde{F}^l = S_r \phi^s \phi^l, \tag{7.13}$$

$$\tilde{F}^s = -S_r \phi^s \phi^l, \tag{7.14}$$

respectively. Rather than being a non-dimensional constant (as in Gray & Thornton 2005; Gray & Chugunov 2006), the non-dimensional segregation rate  $S_r$  is a function, whose value varies locally in the flow, and which is given by (7.8).

Figure 12(a) shows a series of flux curves for different size ratios  $R$ , assuming that  $\hat{z} = 1/2$ ,  $d_s = 4$  mm and the non-dimensional coefficients in table 3. All the flux curves are asymmetric and have an inflection point that lies to the right of the maximum. Qualitatively they look similar to the cubic flux functions for  $\chi > 1/2$  illustrated in figure 1. Crucially, however, these curves have been derived to quantitatively match experimental data and contain complex functional dependencies on the shear rate, the local small particle concentration, the average grain size, the grain-size ratio and the local pressure. In particular, as the grain-size ratio is increased the amplitude of the flux function increases and both the local maximum and the inflection point move to the left.

The increasing skewness with grain-size ratio encodes the idea that small intruders find it increasingly easy to percolate downwards as the size ratio increases, whereas the large intruders find it harder to segregate upwards when there are more contacts with neighbouring small particles. The flux curves have this asymmetric behaviour even when  $\mathcal{C} = 0$  and  $\mathcal{E} = 0$ , indicating that the scaling of the segregation rate on the mean particle diameter  $\bar{d}$  in (4.9) is already sufficient to produce this effect. The flux curves look similar at other heights in the flow and grow in amplitude as one approaches the free surface. When  $\mathcal{C} \neq 0$  there is an upper bound for the amplitude at  $\hat{z} = 1$ , but when  $\mathcal{C} = 0$  the segregation flux becomes unbounded at the free surface, which is not desired.

#### 7.4. Large and small particle segregation velocities

In the absence of diffusion the non-dimensional vertical velocities of the large and small particles are given by

$$\tilde{w}^l = S_r \phi^s, \tag{7.15}$$

$$\tilde{w}^s = -S_r \phi^l, \tag{7.16}$$

respectively. These are plotted in figure 12(b) for the same size ratios and parameters as the flux functions in figure 12(a). For a given size ratio, the downward small particle segregation velocity is an increasing function of the large particle concentration  $\phi^l = 1 - \phi^s$ , and therefore the maximum speed is attained at  $\phi^s = 0^+$ . Conversely, the large particles have a local maximum segregation velocity at an intermediate concentration  $\phi^s \in (0, 1)$ , with the segregation velocity of a single large intruder at  $\phi^s = 1^-$  being at a much reduced rate, compared to either the maximum large particle, or the maximum small particle, segregation speed. Experimental measurements of the single intruder end states have been specifically used in this paper to determine the scaling law for segregation, and hence the segregation rate  $S_r$ . The particle velocities in these end states are therefore a close match to the experimental data.

It is interesting to note that when  $\mathcal{C} = 0$ , the ratio of the maximum percolation velocity of a single small intruder to the rise velocity of a single large intruder at a given height  $\hat{z}_0$ , satisfies the simple relation

$$\left. \frac{|\tilde{w}^s(0^+)|}{|\tilde{w}^l(1^-)|} \right|_{\hat{z}=\hat{z}_0} = \left. \frac{S_r(0^+)}{S_r(1^-)} \right|_{\hat{z}=\hat{z}_0} = R^2 (1 + \mathcal{E}(R - 1)). \tag{7.17}$$

The remarkable equation relates two seemingly disparate ends of the flux curve with a simple relation that is purely dependent on the particle size ratio  $R$ . It holds at all heights  $\hat{z}_0$  in the flow, which implies that the trajectories of the particles are also related. In particular, it follows from (4.15) and (4.19) that the ratio of the time  $t_l$  for a large intruder to reach the top of the cell, and the time  $t_s$  for a small intruder to percolate down to the base, satisfies the same law

$$\frac{t_l}{t_s} = R^2 (1 + \mathcal{E}(R - 1)). \tag{7.18}$$

Even when  $\mathcal{C} = 0.2712$ , and there is some dependence on the average grain size and the position in the flow, (7.17) and (7.18) provide good approximations to the ratio of the single particle intruder speeds and the ratio of intruder times, respectively.

#### 7.5. Comparison to van der Vaart's (2015) experimental data

Van der Vaart *et al.* (2015) used an earlier version of the shear cell and the RIM technique to measure the evolution of the particle-size distribution in a 50 : 50 mix of 8 mm and

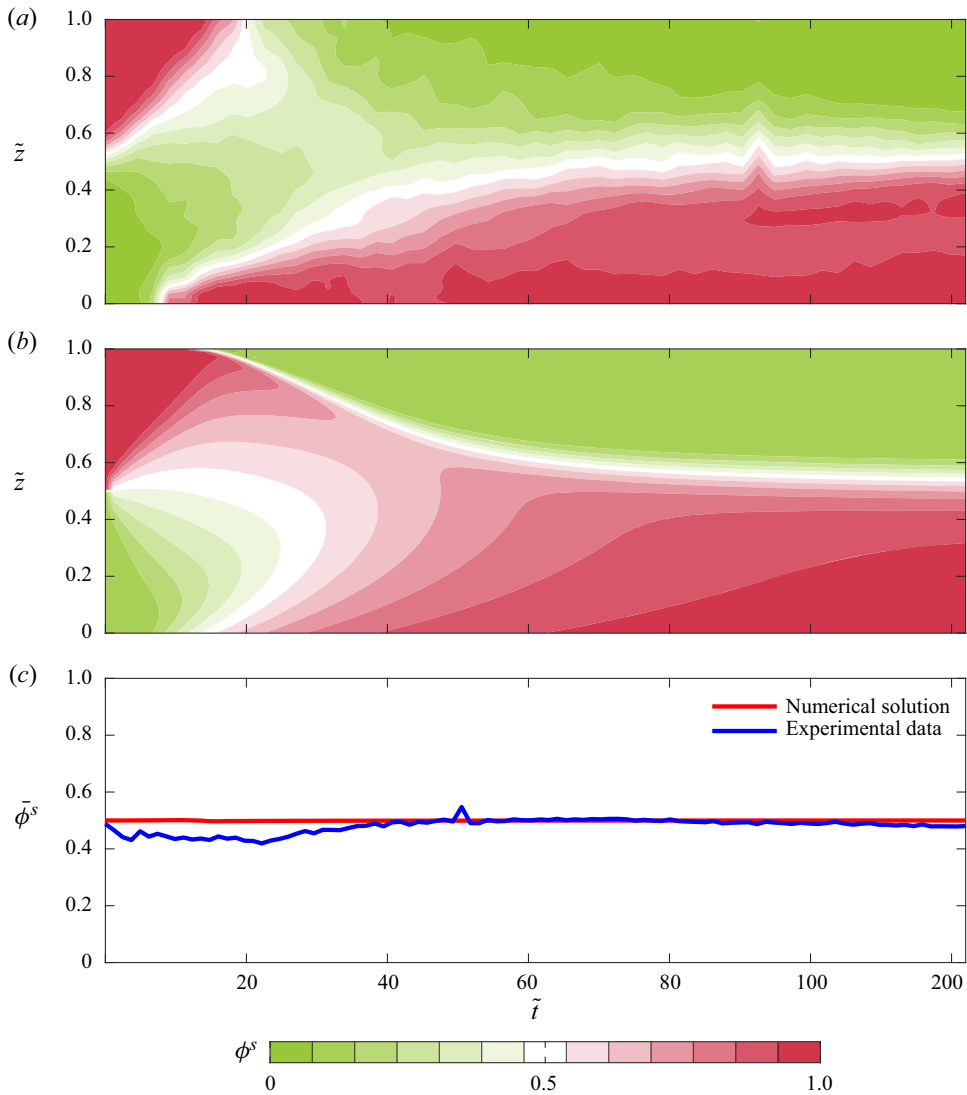


Figure 13. (a) Contour plot of van der Vaart *et al.*'s (2015) small particle concentration data as a function of the non-dimensional depth  $\tilde{z} = z/h$  and non-dimensional time  $\tilde{t} = t/T$ , for a 50 : 50 mix of large and small particles with  $h = 87$  mm,  $T = 13$  s,  $\theta_{max} = 30^\circ$ ,  $d_s = 4$  mm and  $d_l = 8$  mm. (b) Contour plot of the corresponding numerical results using the non-dimensional coefficients summarized in table 3. (c) Experimental and numerical time series of the depth-averaged concentration of small particles,  $\bar{\phi}^s = \bar{\phi}^s(t)$ .

4 mm particles that was initially in a normally graded configuration. To do this, the shear was stopped after each complete cycle and the cell was scanned with a laser while a series of photographs were taken. From these photos it was possible to determine the three-dimensional particle positions after each cycle and hence to build up a picture of the evolving particle-size distribution in time. A space-time plot of the van der Vaart *et al.*'s (2015) small particle concentration data is shown in figure 13(a).

Figure 13(b) shows a contour plot of the computed small particle concentration as a function of the non-dimensional depth and time, using the experimentally determined non-dimensional coefficients in table 3. The simulations are in very good quantitative

agreement with the experimental data of van der Vaart *et al.* (2015). In particular, they accurately capture the time at which the first small grains reach the base of the flow, the slightly later arrival of the first large grains at the top of the flow, as well as the overall time scale for the solution to approach the steady state by  $\tilde{t} = 120$ . During this evolution the grains reverse position, with the large particles rising to the surface and the small grains percolating down to the base, to form a slightly diffuse inversely graded particle-size distribution. It should be emphasized that this excellent overall agreement is achieved with the value of  $\mathcal{A}$  determined from the experiments of Utter & Behringer (2004) and the same non-dimensional coefficients  $\mathcal{B}$ ,  $\mathcal{C}$  or  $\mathcal{E}$  measured in this paper, together with the simplest possible functional form for  $\Lambda$ .

The slight mismatches between the simulated and experimental concentration contours in the expansion fan, between  $\tilde{t} = 0$  and 60 time units, are most likely due to experimental error. To demonstrate this, it is useful to integrate the segregation equation (7.7) from the base up to the free surface, and apply the surface and basal no flux boundary conditions (7.11). Exchanging the order of integration and differentiation implies that

$$\frac{d}{d\tilde{t}} \left( \int_0^1 \phi^s d\tilde{z} \right) = 0, \tag{7.19}$$

and hence that the depth-averaged concentration of small particles is conserved, i.e.

$$\bar{\phi}^s = \int_0^1 \phi^s(\tilde{z}, \tilde{t}) d\tilde{z} = \int_0^1 \phi^s(\tilde{z}, 0) d\tilde{z} = \bar{\phi}_0^s. \tag{7.20}$$

Figure 13(c) shows the depth-averaged concentration  $\bar{\phi}^s$  as a function of time for the numerical simulation and the experiment. While the simulated  $\bar{\phi}^s$  is indeed constant, and equal to the initial depth-averaged concentration of small particle  $\bar{\phi}_0^s = 0.5$ , the experimental value of  $\bar{\phi}^s$  is up to 5% below this value in the first  $\tilde{t} = 0$  and 60 time units. This is due to the error in identifying all the small particles with the refractive-index matched fluid technique used by van der Vaart *et al.* (2015).

### 7.6. Properties of the steady-state solution

A first-order ODE for the steady-state concentration profile can be formulated by assuming that the concentration is independent of time. Integrating the non-dimensional segregation equation (7.7) with respect to  $\tilde{z}$ , applying the no flux condition (7.11) and cancelling the  $\dot{\gamma}T(\bar{d}/h)^2$  dependence yields

$$\frac{d\phi^s}{d\tilde{z}} = -\frac{(\mathcal{B}/\mathcal{A})\phi^s\phi^l\mathcal{F}(R, \phi^s)}{\mathcal{C}(\bar{d}/h) + \Phi(1 - \tilde{z})}. \tag{7.21}$$

This equation has some interesting properties. In particular, the non-dimensional coefficient  $\mathcal{C}$  is included in the theory primarily to remove the singularity in the segregation rate at the free surface in the numerical method. When  $\mathcal{C} = 0$ , (7.21) just depends on the particle size ratio  $R$ , and is completely independent of  $\bar{d}$  and  $h$ . The thickness does enter in the non-dimensionalization (7.6a,b), so although the non-dimensional solution will be identical for a fixed size ratio, the physical solution will be stretched vertically proportionately to  $h$ . As a result, a flow of double the thickness will have steady-state concentration gradients that are half as strong as the original flow for the same size ratio. This is a highly non-intuitive consequence of the combination of the scaling law (7.2) and the diffusivity (7.5), and is a bold prediction of the resulting theory.

7.7. Exact steady-state solution for the case  $\mathcal{C} = 0$

In the case when  $\mathcal{C} = 0$ , it is possible to derive an exact steady-state solution to (7.21). Substituting (7.3) and (7.4) into (7.21) and writing it as an ODE for  $\tilde{z} = \tilde{z}(\phi^s)$  implies

$$\frac{-1}{(1 - \tilde{z})} \frac{d\tilde{z}}{d\phi^s} = \frac{\mathcal{A}\Phi}{\mathcal{B}(R - 1)\phi^s(1 - \phi^s)[1 + \mathcal{E}(1 - \phi^s)(R - 1)]}. \tag{7.22}$$

Using partial fractions the right-hand side can be integrated to give the exact solution

$$\tilde{z} = 1 - K(1 - \phi^s)^{-\lambda_1} (1 + \mathcal{E}(1 - \phi^s)(R - 1))^{\lambda_2} (\phi^s)^{\lambda_3}, \tag{7.23}$$

where  $K$  is a constant of integration and the coefficients  $\lambda_1$ ,  $\lambda_2$  and  $\lambda_3$  are

$$\lambda_1 = \frac{\Phi\mathcal{A}}{\mathcal{B}(R - 1)}, \quad \lambda_2 = \frac{\Phi\mathcal{A}\mathcal{E}}{\mathcal{B}(1 + \mathcal{E}(R - 1))}, \quad \lambda_3 = \frac{\Phi\mathcal{A}}{\mathcal{B}(R - 1)(1 + \mathcal{E}(R - 1))}, \tag{7.24a-c}$$

respectively. The average volume fraction of small particles in the cell is obtained by integrating the area under the curve  $\phi^s = \phi^s(\tilde{z})$  between  $\tilde{z}$  is zero and unity. Since, this area is exactly the same as the area under the curve  $\tilde{z} = \tilde{z}(\phi^s) > 0$  in the range  $\phi^s = [0, 1]$ , it is easy to find the constant of integration for any given average concentration of small particles in the cell.

7.8. Steady-state comparison to van der Vaart’s (2015) experiment

Figure 14 shows the predicted steady-state exact solution for the experiment of van der Vaart *et al.* (2015), where  $K = 0.4041$  for the initial 50 : 50 mix of particles. At  $\hat{t} = 221$  non-dimensional units the exact solution lies very close to the computed concentration profile using the non-zero value of  $\mathcal{C} = 0.2712$  determined in this paper. In fact both the curves lie very close to van der Vaart *et al.*’s (2015) experimental data between 177 and 221 cycles, when the experiment is essentially in steady state (see figure 14). Following Wiederseiner *et al.* (2011) and Gray (2018), the Péclet number for segregation is defined as the ratio of the non-dimensional segregation rate to the rate of non-dimensional diffusion, i.e.

$$Pe = \frac{S_r}{D_r} = \frac{\mathcal{B}(R - 1)(1 + \mathcal{E}(1 - \phi^s)(R - 1))}{\mathcal{A}(\mathcal{C}(\bar{d}/h) + \Phi(1 - \tilde{z}))}. \tag{7.25}$$

It provides a measure of the strength of the segregation relative to the diffusion. As opposed to some earlier theories (see e.g. Gray & Chugunov 2006; Wiederseiner *et al.* 2011), which had a constant Péclet number, the segregation model developed in this paper produces a Péclet number that varies strongly with depth. This is due to the changing local grain-size distribution and the decreasing lithostatic pressure distribution with increasing height. For the computed solution (see inset figure 14) the Péclet number starts at  $Pe = 5.74$  at the base of the flow, rises to  $Pe = 18.86$  at  $\tilde{z} = 1/2$  and then tends to a finite, but, large, value of  $Pe = 430$  at the top. Note that in the case when  $\mathcal{C} = 0$ , the Péclet number will be similar over most of the range, but the singularity in pressure at the free-surface implies that  $Pe \rightarrow \infty$  at  $\tilde{z} \rightarrow 1$ . Since the diffuse interface separating high concentrations of large particles from high concentrations of fines, in figure 14, lies between  $\tilde{z} = 0.4$  and  $0.6$ , the Péclet number  $Pe = 11.38$  at the lower end of this range and rises sharply to  $Pe = 37$  near the top. As a result, the solution is much more rounded and diffuse at the bottom, which is a defining feature of the current theory.

Downloaded from https://www.cambridge.org/core. IP address: 78.147.81.167, on 20 Apr 2021 at 14:57:36, subject to the Cambridge Core terms of use, available at https://www.cambridge.org/core/terms. https://doi.org/10.1017/jfm.2021.221

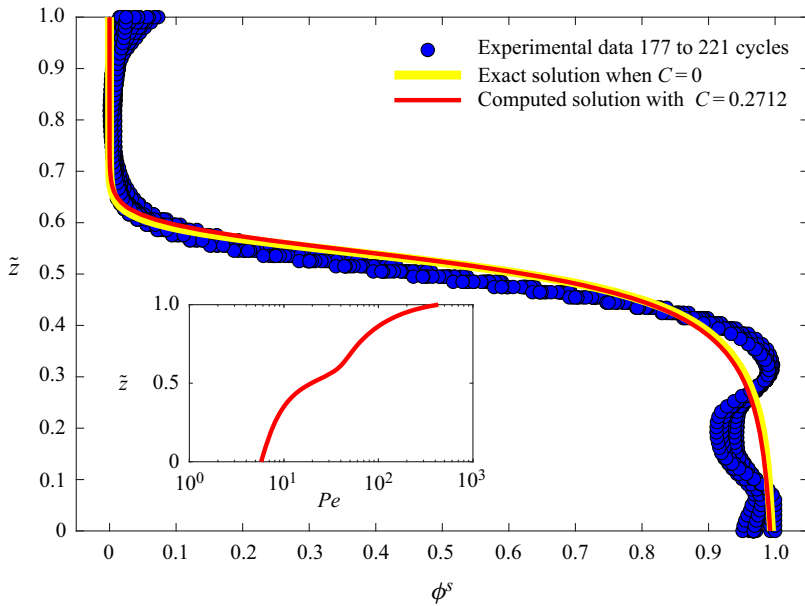


Figure 14. Plot of the computed small concentration  $\phi^s$  at  $\tilde{t} = 221$  non-dimensional time units (red line) as a function of the non-dimensional depth, for  $h = 87$  mm,  $T = 13$  s,  $\theta_{max} = 30^\circ$ ,  $d_s = 4$  mm,  $d_l = 8$  mm and using the non-dimensional coefficients summarized in table 3. The blue circles show the corresponding experimental data of van der Vaart *et al.* (2015) between  $\hat{t} = 177$  and 221 non-dimensional time units (cycles). The yellow curve shows the exact steady-state solution (when  $C = 0$ ) with a constant of integration  $K = 0.4041$  for a 50 : 50 mix of particles as in van der Vaart *et al.*'s (2015) experiments. The inset image shows the variation of the Péclet number with depth for the computed solution when  $C \neq 0$ .

## 8. Predicting maximum segregation at a grain-size ratio close to two

Golick & Daniels (2009) and Thornton *et al.* (2012) provide experimental and DPM simulation evidence, which strongly suggests that maximum segregation occurs close to a grain-size ratio of two for a 50 : 50 mixture of large and small particles (see data in figure 15). At first sight, this appears to be incompatible with the experimental shear box results presented here, where the segregation velocity magnitude  $f_{sl}$  increases linearly with  $R - 1$  for both large and small intruders, and where there is an additional  $(R - 1)^2$  dependence for the small intruders at high grain-size ratios. In short, the shear box data show no evidence of a maximum in the segregation at a grain-size ratio of two. One may therefore legitimately ask how these results can be compatible with one another?

In contrast to the prescribed motion and shear rate in our experiments, Golick & Daniels (2009) and Thornton *et al.* (2012) consider rapid flows in which segregation, diffusion and advection actively contribute to the evolving particle-size distribution, i.e. they are inherently more complex coupled flows. In particular, the velocity profile  $u(z, t)$ , shear rate  $\dot{\gamma}(z, t)$  and solids volume fraction  $\Phi(z, t)$  are functions of space and time. In chute flows, Rognon *et al.* (2007), Tripathi & Khakhar (2011) and Barker *et al.* (2021) have shown that segregation-induced frictional feedbacks are responsible for marked deviations away from the classical monodisperse Bagnold velocity profile (Silbert *et al.* 2001; GDR-MiDi 2004; Jop *et al.* 2006). These feedbacks will in turn change the local shear rate and hence the time scale for particles to segregate and diffuse. In addition, mixtures of disparately sized particles can pack more efficiently than monodisperse grains even during shear (Golick & Daniels 2009; Thornton *et al.* 2012). This packing effect is so significant in Golick &

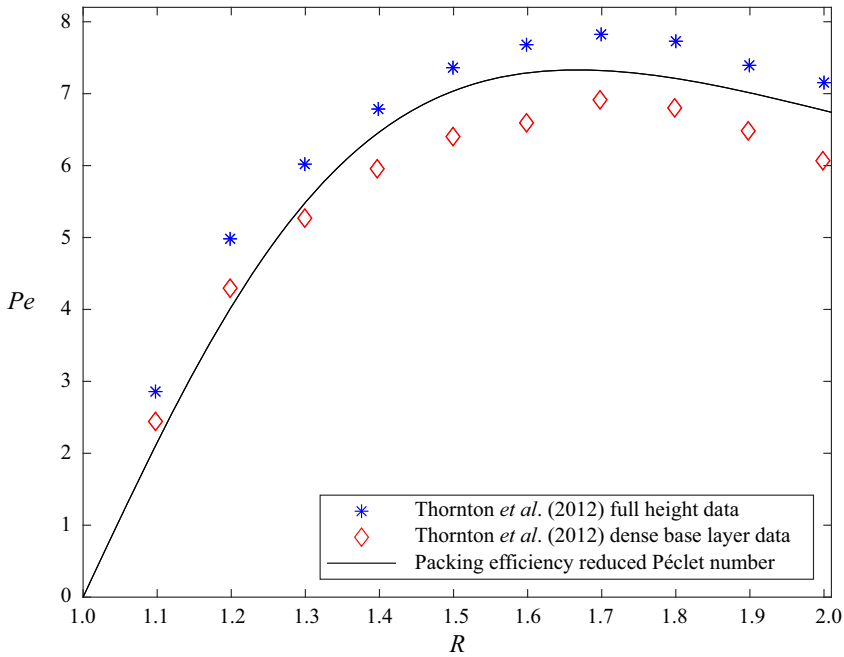


Figure 15. A comparison of the packing efficiency reduced Péclet number (8.3) as a function of the grain-size ratio  $R$ , with the DPM simulation results of Thornton *et al.* (2012). The Péclet number is evaluated at  $\tilde{z} = 0.5$  and  $\phi^s = 0.5$  to approximate the position and concentration along the smooth steady-state interface between large and small grains in a 50 : 50 mix. The transition  $\phi_c^s = 0.2$ , so the factor  $\Lambda$  is zero, and for simplicity  $C = 0$ . To account for the absence of an interstitial fluid, the constant  $B$  is divided by a buoyancy factor (4.10) using the  $\rho_* = 2.2 \text{ g cm}^{-3}$  and  $\rho_*^f = 1.044 \text{ g cm}^{-3}$  for the intrinsic density of the grains and the fluid, respectively (table 1). This determines the initial linear gradient of the Péclet number at grain-size ratios close to unity. A remarkably good fit to Thornton *et al.*'s (2012) DPM data is provided by setting the constant  $a = 9$  in the segregation reduction factor (8.2). In particular, it produces a maximum in the Péclet number at a grain-size ratio  $R \simeq 1.66$ .

Daniels' (2009) annular shear-cell experiments, that they used the motion of the freely moving top plate to infer the segregation time scale. If the solids volume fraction is locally enhanced, then this reduces the number of gaps that particles can move into and provides a natural mechanism for reducing both the segregation rate and the diffusivity. The observed maximum in segregation in the vicinity of  $R = 2$  may therefore be a consequence of increased solids volume fraction, or frictional feedback, rather than a direct dependence of segregation velocity magnitude  $f_{sl}$  on the grain-size ratio  $R$ .

It is instructive to consider how packing effects may be parameterized in a simple way, without developing a compressible theory for particle-size segregation that fully accounts for the changes in solids volume fraction. To begin, let us assume that the  $(1 - R)^2$  enhancement of segregation, as one approaches the transition to spontaneous percolation (Bridgwater & Ingram 1971; Wilkinson & Edwards 1982), is confined to low small particle concentrations. This effect can be achieved by defining

$$\Lambda = \begin{cases} 1 - \frac{\phi^s}{\phi_c^s}, & \phi \leq \phi_c^s \\ 0, & \phi^s > \phi_c^s, \end{cases} \quad (8.1)$$

where the transition point  $\phi_c^s \in (0, 1)$ . There are two key ideas that the function must parameterize: (i) grains can only pack together more efficiently when they are mixed together and (ii) this effect becomes progressively stronger as the grain-size ratio increases from unity. A packing-induced segregation reduction factor might therefore take the form

$$\mathcal{R} = 1 + a(R - 1)^2 \phi^s (1 - \phi^s), \quad (8.2)$$

where  $a$  is a constant. This factor enters the denominator of the Péclet number (7.25) to give a packing efficiency reduced Péclet number of the form

$$Pe = \frac{\mathcal{B}(R - 1)(1 + \mathcal{E}\Lambda(\phi^s)(R - 1))}{\mathcal{A}\mathcal{R}(\phi^s, R)(C(\bar{d}/h) + \Phi(1 - \tilde{z}))}. \quad (8.3)$$

The reduction factor  $\mathcal{R}$  is equal to unity at  $\phi^s = 0, 1$ , so our single-intruder results are encapsulated unchanged in this function. However, at intermediate concentrations  $\phi^s > \phi_c^s$  the Péclet number is reduced when either the grain-size ratio  $R$  is increased, or the mixture concentration approaches  $\phi^s = 0.5$ . Figure 15 shows that the reduction factor (8.2) accurately captures Thornton *et al.*'s (2012) steady-state Péclet number dependence on  $R$ , with a maximum segregation at a grain-size ratio  $R \simeq 1.66$ . This is remarkably close to the maximum at  $R = 1.7$  in Thornton *et al.*'s (2012) DPM simulations, which is very encouraging. The fact that Golick & Daniels' (2009) annular shear-cell experiments have a minimum segregation time at  $R \simeq 2$ , suggests that this factor reduces the segregation velocity magnitude, rather than the diffusion. However, it is possible that the increased solids volume fraction in mixtures of differently sized particles also moderates the self-diffusion, and that (8.2) is the net effect of the reduction in segregation and the reduction or enhancement in diffusion.

Other effects such as the intermediate and reverse segregation reported by Thomas (2000) and Thomas & D'Ortona (2019) at very large size ratios  $R > 4$  probably require an additional effective density effect to explain them. To see this, consider filling the volume of a large grain with smaller particles. As they randomly pack together to fill the volume they will introduce a significant amount of empty space. At the large particle scale, it follows that very large intruders will appear significantly denser than an equivalent volume of small grains, even if their intrinsic densities are the same. This apparent density increase may thus lead to a competition between particle size and particle density segregation (Tunuguntla *et al.* 2014; Gray & Ancy 2015), which combined with flow feedback and packing efficiency effects may explain how very large intruders can find equilibria at intermediate depths, or sink to the base of the flow.

## 9. Conclusions

The refractive-index matched shear box experiments performed in this paper suggest a simple functional form (4.9) for the segregation velocity magnitudes  $f_{sl}$  of single large and small intruders. For grain-size ratios close to unity, a simple linear interpolation (7.4) between these two end states is sufficient to quantitatively model the segregation of a 50 : 50 mix of large and small particles in the shear box experiments of van der Vaart *et al.* (2015), when it is combined with the generalized diffusivity (4.22) (see figures 13 and 14). At larger size ratios the annular shear-cell experiments of Golick & Daniels (2009) suggest that mixtures of grains can pack at significantly higher solids volume fractions, even during shear, and that this hinders the small particles ability to percolate and segregate. By introducing a simple parametrization of this reduced segregation efficiency (8.2), it is possible to produce a maximum Péclet number for segregation at a grain-size ratio

$R \simeq 1.66$ . This is remarkably close to the maximum at  $R = 1.7$  found in the steady-state DPM simulations of Thornton *et al.* (2012). The composite small particle segregation flux (2.7) that includes all of these effects, is then

$$F^s = \left( \frac{\hat{\rho} \hat{B} \rho_* \dot{\gamma} \bar{d}^2}{C \rho_* g \bar{d} + p} \right) \frac{[(R - 1) + \mathcal{E} \Lambda(\phi^s)(R - 1)^2]}{\mathcal{R}(\phi^s, R)} \phi^s \phi^l \mathbf{g}, \quad (9.1)$$

where the relative density difference  $\hat{\rho}$  defined in (4.10) accounts for the presence of an interstitial fluid of density  $\rho_*^f$ , and the correspondingly adjusted constant  $\hat{B} = B/\hat{\rho} \simeq 0.7125$ . The remaining values of the universal constants can be found in table 3. The small particle segregation flux is dependent of the shear rate  $\dot{\gamma}$ , the local mean particle size  $\bar{d}$ , the intrinsic density of the grains  $\rho_*$ , the pressure  $p$ , the size ratio  $R$ , the gravitational acceleration vector  $\mathbf{g}$  and the local concentration of small particles  $\phi^s = 1 - \phi^l$ . The dependence on the average particle size  $\bar{d}$  naturally leads to increasingly asymmetric flux functions as the size ratio  $R$  increases (Gajjar & Gray 2014; van der Vaart *et al.* 2015). This leads to markedly different time scales for the rise and fall of large and small intruders, as shown theoretically in figure 12.

Particle-size segregation usually takes place in rapidly sheared free-surface flows, where the pressure is lithostatic. Interestingly, when the pressure distribution (4.13) is substituted into (9.1) the intrinsic density dependence and the magnitude of the gravitational acceleration  $g = |\mathbf{g}|$  cancel out, to leave the segregation flux

$$F^s = \left( \frac{\hat{\rho} \hat{B} \dot{\gamma} \bar{d}^2}{C \bar{d} + \Phi(h - z)} \right) \frac{[(R - 1) + \mathcal{E} \Lambda(\phi^s)(R - 1)^2]}{\mathcal{R}(\phi^s, R)} \phi^s \phi^l \check{\mathbf{g}}, \quad (9.2)$$

where  $\check{\mathbf{g}} = \mathbf{g}/|\mathbf{g}|$  is the unit vector in the direction of gravity. This implies that gravity sets the direction for segregation, but it does not determine the time scale for particles to segregate. This is consistent with Savage & Lun's (1988) statistical model for kinetic sieving and squeeze expulsion, in which the shear rate sets the time scale for segregation, as it determines the rate at which small particles see gaps that they can percolate down into during the kinetic sieving process. The percolation velocity of a single small intruder has a linear dependence on  $R - 1$  for size ratios close to unity, but develops a quadratic dependence at higher grain-size ratios as shown in the inset in figure 10. This is probably related to the transition to spontaneous percolation for grain-size ratios greater than six (Bridgwater & Ingram 1971; Wilkinson & Edwards 1982). This effect may be confined to relatively low concentrations of fine particles, since at larger concentrations the pores will be blocked. The function  $\Lambda$  defined in (8.1) restricts enhanced percolation to  $\phi^s \in [0, \phi_c^s]$ , where  $\phi_c^s < 1$ . There are, however, independent DPM simulations (Chassagne *et al.* 2020) that support the linear and quadratic dependence on  $R - 1$  proposed here.

The ability of the theory to match all the existing experiments that have been performed in the oscillating shear cell, as well as Thornton *et al.*'s (2012) steady-state DPM simulations, suggests that the empirical segregation flux (9.1) might usefully be applied to other problems. Certainly, the theory has the right pressure dependence in the segregation and diffusion terms to capture the suppression of segregation in Golick & Daniels' (2009) annular shear-cell experiments, and Fry *et al.*'s (2019) DPM simulations, when a weight is added to the top plate. In addition, Barker *et al.* (2021) have coupled the empirical segregation law (9.1) to the partially regularized  $\mu(I)$ -rheology (Barker & Gray 2017), and used it to compute the segregation in a square rotating drum. The results show that the empirical law can capture the qualitative development of the segregation patterns that form in the drum. Quantitative comparison with experiments is much more difficult than

one might expect, because sidewall wall friction significantly influences the depth and speed of the surface avalanche where most of the segregation occurs. For the same rotation rate, a narrow drum produces a much thinner faster moving avalanche than a wide drum (Jop, Forterre & Pouliquen 2005). As a result, the shear rate is higher and the pressure is lower in a narrow drum, and both of these effects combine to increase the segregation rate according to (9.1). It is therefore vital to include sidewall friction in numerical simulations, in order to make a proper comparison to experimental patterns observed through the sidewall of narrow drums.

The fully coupled simulations of Barker *et al.* (2021) make it clear that one of the key advantages of the oscillatory shear cell is that the bulk motion of the grains is prescribed rather than being free to evolve as part of the experiment. This eliminates many of the problems posed by sidewall friction (Jop *et al.* 2005) as well as the more subtle feedback of the evolving particle-size distribution on the bulk flow field (see e.g. Tripathi & Khakhar 2011; Barker *et al.* 2021). It is this uncoupling which makes it much easier to determine the underlying functional dependence of the segregation rate in the shear cell.

**Supplementary movies.** Supplementary movies are available at <https://doi.org/10.1017/jfm.2021.227>.

**Acknowledgements.** The authors would like to thank B. de Graffenried for designing and building the new experimental shear cell, as well as for taking some of the photographs in this paper. All the data used for plotting figures 5–15 are archived at Zenodo (<https://doi.org/10.5281/zenodo.4597441>).

**Funding.** We acknowledge the support of the Swiss National Science Foundation through Project 200020 175750 and the Swiss Federal Commission for Scholarships. This research was also supported by NERC grants NE/E003206/1 and NE/K003011/1 as well as EPSRC grants EP/I019189/1, EP/K00428X/1 and EP/M022447/1. J.M.N.T.G. is a Royal Society Wolfson Research Merit Award holder (WM150058) and an EPSRC Established Career Fellow (EP/M022447/1).

**Declaration of interests.** The authors report no conflict of interest.

#### Author ORCIDs.

-  T. Trehwela <https://orcid.org/0000-0002-7461-8570>;
-  C. Ancey <https://orcid.org/0000-0003-3354-7398>;
-  J.M.N.T. Gray <https://orcid.org/0000-0003-3554-0499>.

#### REFERENCES

- BAKER, J.L., JOHNSON, C.G. & GRAY, J.M.N.T. 2016 Segregation-induced finger formation in granular free-surface flows. *J. Fluid Mech.* **809**, 168–212.
- BARKER, T. & GRAY, J.M.N.T. 2017 Partial regularisation of the incompressible  $\mu(I)$ -rheology for granular flow. *J. Fluid Mech.* **828**, 5–32.
- BARKER, T., RAUTER, M., MAGUIRE, E., JOHNSON, C. & GRAY, J.M.N.T. 2021 Coupling rheology and segregation in granular flows. *J. Fluid Mech.* **909**, A22.
- BARKER, T., SCHAEFFER, D.G., SHEARER, M. & GRAY, J.M.N.T. 2017 Well-posed continuum equations for granular flow with compressibility and  $\mu(I)$ -rheology. *Proc. R. Soc. A* **473**, 20160846.
- BATES, L. 1997 *User Guide to Segregation*. British Materials Handling Board.
- BAXTER, J., TÜZÜN, U., HEYES, D., HAYATI, I. & FREDLUND, P. 1998 Stratification in poured granular heaps. *Nature* **391**, 136.
- BRIDGWATER, J., FOO, W. & STEPHENS, D. 1985 Particle mixing and segregation in failure zones – theory and experiment. *Powder Technol.* **41**, 147.
- BRIDGWATER, J. & INGRAM, N. 1971 Rate of spontaneous inter-particle percolation. *Trans. Inst. Chem. Engng* **49**, 163–169.
- CHASSAGNE, R., MAURIN, R., CHAUCHAT, J., GRAY, J.M.N.T. & FREY, P. 2020 Discrete and continuum modelling of grain size segregation during bedload transport. *J. Fluid Mech.* **895**, A30.
- CHEN, K.-D., LIN, Y.-F. & TU, C.-H. 2012 Densities, viscosities, refractive indexes, and surface tensions for mixtures of ethanol, benzyl acetate, and benzyl alcohol. *J. Chem. Engng Data* **57** (4), 1118–1127.

- CROCKER, J.C. & GRIER, D.G. 1996 Methods of digital video microscopy for colloidal studies. *J. Colloid Interface Sci.* **179** (1), 298–310.
- DENISSEN, I., WEINHART, T., TE VOORTWIS, A.S., GRAY, S.L. & THORNTON, A.R. 2019 Bulbous head formation in bidisperse shallow granular flow over an inclined plane. *J. Fluid Mech.* **866**, 263–297.
- DOLGUNIN, V.N. & UKOLOV, A.A. 1995 Segregation modelling of particle rapid gravity flow. *Powder Technol.* **83**, 95–103.
- FAN, Y., BOUKERKOUR, Y., BLANC, T., UMBANHOWAR, P.B., OTTINO, J.M. & LUEPTOW, R.M. 2012 Stratification, segregation, and mixing of granular materials in quasi-two-dimensional bounded heaps. *Phys. Rev. E* **86**, 051305.
- FAN, Y., SCHLICK, C.P., UMBANHOWAR, P.B., OTTINO, J.M. & LUEPTOW, R.M. 2014 Modelling size segregation of granular materials: the roles of segregation, advection and diffusion. *J. Fluid Mech.* **741**, 252–279.
- FRY, A.M., UMBANHOWAR, P.B., OTTINO, J.M. & LUEPTOW, R.M. 2019 Diffusion, mixing, and segregation in confined granular flows. *AIChE J.* **65**, 875–881.
- GAJJAR, P. & GRAY, J.M.N.T. 2014 Asymmetric flux models for particle-size segregation in granular avalanches. *J. Fluid Mech.* **757**, 297–329.
- GDR-MiDi 2004 On dense granular flows. *Eur. Phys. J. E* **14**, 341–365.
- GILBERG, D. & STEINER, K. 2020 Size segregation in compressible granular shear flows of binary particle systems. *Granul. Matter* **22**, 45.
- GODDARD, J.D. & LEE, J. 2018 Regularization by compressibility of the  $\mu(I)$  model of dense granular flow. *Phys. Fluids* **30**, 073302.
- GOLICK, L.A. & DANIELS, K.E. 2009 Mixing and segregation rates in sheared granular materials. *Phys. Rev. E* **80** (4), 042301.
- GRAY, J.M.N.T. 2018 Particle segregation in dense granular flows. *Annu. Rev. Fluid Mech.* **50**, 407–433.
- GRAY, J.M.N.T. & ANCEY, C. 2011 Multi-component particle size segregation in shallow granular avalanches. *J. Fluid Mech.* **678**, 535–588.
- GRAY, J.M.N.T. & ANCEY, C. 2015 Particle-size and particle-density segregation in granular avalanches. *J. Fluid Mech.* **779**, 622–668.
- GRAY, J.M.N.T. & CHUGUNOV, V.A. 2006 Particle-size segregation and diffusive remixing in shallow granular avalanches. *J. Fluid Mech.* **569**, 365–398.
- GRAY, J.M.N.T. & HUTTER, K. 1997 Pattern formation in granular avalanches. *Continuum Mech. Thermodyn.* **9**, 341–345.
- GRAY, J.M.N.T. & THORNTON, A.R. 2005 A theory for particle size segregation in shallow granular free-surface flows. *Proc. R. Soc. A* **461**, 1447–1473.
- GRAY, J.M.N.T., WIELAND, M. & HUTTER, K. 1999 Free surface flow of cohesionless granular avalanches over complex basal topography. *Proc. R. Soc. A* **455**, 1841–1874.
- GUILLARD, F., FORTERRE, Y. & POULIQUEN, O. 2016 Scaling laws for segregation forces in dense sheared granular flows. *J. Fluid Mech.* **807**, R1.
- HILL, K.M., KHARKAR, D.V., GILCHRIST, J.F., MCCARTHY, J.J. & OTTINO, J.M. 1999 Segregation driven organization in chaotic granular flows. *Proc. Natl Acad. Sci. USA* **96**, 11701–11706.
- ISNER, A.B., UMBANHOWAR, P.B., OTTINO, J.M. & LUEPTOW, R.M. 2020 Axisymmetric granular flow on a bounded conical heap: kinematics and size segregation. *Chem. Engng Sci.* **217**, 115505.
- IVERSON, R.M. & VALLANCE, J.W. 2001 New views of granular mass flows. *Geology* **29** (2), 115–118.
- JING, L., KWOK, C.Y. & LEUNG, Y.F. 2017 Micromechanical origin of particle size segregation. *Phys. Rev. Lett.* **118**, 118001.
- JOHANSON, J.R. 1978 Particle segregation . . . and what to do about it. *Chem. Engng* **85**, 183–188.
- JONES, R.P., ISNER, A.B., XIAO, H., OTTINO, J.M., UMBANHOWAR, P.B. & LUEPTOW, R.M. 2018 Asymmetric concentration dependence of segregation fluxes in granular flows. *Phys. Rev. Fluids* **3**, 094304.
- JOP, P., FORTERRE, Y. & POULIQUEN, O. 2005 Crucial role of sidewalls in granular surface flows: consequences for the rheology. *J. Fluid Mech.* **541**, 167–192.
- JOP, P., FORTERRE, Y. & POULIQUEN, O. 2006 A constitutive relation for dense granular flows. *Nature* **44**, 727–730.
- KHAKHAR, D.V., ORPE, A.V. & HAJRA, S.K. 2003 Segregation of granular materials in rotating cylinders. *Physica A* **318**, 129–136.
- LIU, Y., GONZALEZ, M. & WASSGREN, C. 2019 Modeling granular material segregation using a combined finite element method and advection-diffusion-segregation equation model. *Powder Technol.* **346**, 38–48.
- MAY, L.B.H., GOLICK, L.A., PHILLIPS, K.C., SHEARER, M. & DANIELS, K.E. 2010 Shear-driven size segregation of granular materials: modeling and experiment. *Phys. Rev. E* **81** (5), 051301.

## An experimental scaling law for particle-size segregation

- MIDDLETON, G.V. 1970 Experimental studies related to problems of flysch sedimentation. In *Flysch Sedimentology in North America* (ed. J. Lajoie), pp. 253–272. Business and Economics Science Ltd.
- PIERSON, T.C. 1986 Flow behavior of channelized debris flows, Mount St. Helens, Washington. In *Hillslope Processes* (ed. A. D. Abrahams), pp. 269–296. Allen and Unwin, Winchester.
- POULIQUEN, O., DELOUR, J. & SAVAGE, S.B. 1997 Fingering in granular flows. *Nature* **386**, 816–817.
- POULIQUEN, O. & VALLANCE, J.W. 1999 Segregation induced instabilities of granular fronts. *Chaos* **9** (3), 621–630.
- ROCHA, F.M., JOHNSON, C.G. & GRAY, J.M.N.T. 2019 Self-channelisation and levee formation in monodisperse granular flows. *J. Fluid Mech.* **876**, 591–641.
- ROGNON, P.G., ROUX, J.N., NAAIM, M. & CHEVOIR, F. 2007 Dense flows of bidisperse assemblies of disks down an inclined plane. *Phys. Fluids* **19**, 058101.
- SAVAGE, S.B. & HUTTER, K. 1989 The motion of a finite mass of granular material down a rough incline. *J. Fluid Mech.* **199**, 177–215.
- SAVAGE, S.B. & LUN, C.K.K. 1988 Particle size segregation in inclined chute flow of dry cohesionless granular solids. *J. Fluid Mech.* **189**, 311–335.
- SCHAEFFER, D.G., BARKER, T., TSUJI, D., GREMAUD, P., SHEARER, M. & GRAY, J.M.N.T. 2019 Constitutive relations for compressible granular flow in the inertial regime. *J. Fluid Mech.* **874**, 926–951.
- SCHLICK, C.P., FAN, Y., UMBANHOWAR, P.B., OTTINO, J.M. & LUEPTOW, R.M. 2015 Granular segregation in circular tumblers: theoretical model and scaling laws. *J. Fluid Mech.* **765**, 632–652.
- SCHULZE, D. 2008 *Powders and Bulk Solids*. Springer.
- SILBERT, L.E., ERTAS, D., GREST, G.S., HALSEY, T.C., LEVINE, D. & PLIMPTON, S.J. 2001 Granular flow down an inclined plane: bagnold scaling and rheology. *Phys. Rev. E* **64**, 051302.
- SKEEL, R.D. & BERZINS, M. 1990 A method for the spatial discretization of parabolic equations in one space variable. *SIAM J. Sci. Stat. Comput.* **11** (1), 1–32.
- THOMAS, N. 2000 Reverse and intermediate segregation of large beads in dry granular media. *Phys. Rev. E* **62**, 961–974.
- THOMAS, N. & D'ORTONA, U. 2019 Evidence of reverse and intermediate size segregation in dry granular flows down a rough incline. *Phys. Rev. E* **97**, 022903.
- THORNTON, A.R., GRAY, J.M.N.T. & HOGG, A.J. 2006 A three-phase mixture theory for particle size segregation in shallow granular free-surface flows. *J. Fluid Mech.* **550**, 1–25.
- THORNTON, A.R., WEINHART, T., LUDING, S. & BOKHOVE, O. 2012 Modeling of particle size segregation: calibration using the discrete particle method. *Intl J. Mod. Phys. C* **23**, 1240014.
- TRIPATHI, A. & KHAKHAR, D.V. 2011 Numerical simulation of the sedimentation of a sphere in a sheared granular fluid: a granular stokes experiment. *Phys. Rev. Lett.* **107**, 108001.
- TRIPATHI, A. & KHAKHAR, D.V. 2013 Density difference-driven segregation in a dense granular flow. *J. Fluid Mech.* **717**, 643–669.
- TUNUGUNTLA, D.R., BOKHOVE, O. & THORNTON, A.R. 2014 A mixture theory for size and density segregation in shallow granular free-surface flows. *J. Fluid Mech.* **749**, 99–112.
- UTTER, B. & BEHRINGER, R.P. 2004 Self-diffusion in dense granular shear flows. *Phys. Rev. E* **69**, 031308.
- VALLANCE, J.W. & SAVAGE, S.B. 2000 Particle segregation in granular flows down chutes. In *IUTAM Symposium on segregation in granular materials* (ed. A.D. Rosato & D.L. Blackmore), pp. 31–51. Kluwer.
- VAN DER VAART, K., GAJJAR, P., EPELY-CHAUVIN, G., ANDREINI, N., GRAY, J.M.N.T. & ANCEY, C. 2015 Underlying asymmetry within particle size segregation. *Phys. Rev. Lett.* **114**, 238001.
- WIEDERSEINER, S., ANDREINI, N., EPELY-CHAUVIN, G., MOSER, G., MONNEREAU, M., GRAY, J.M.N.T. & ANCEY, C. 2011 Experimental investigation into segregating granular flows down chutes. *Phys. Fluids* **23**, 013301.
- WILKINSON, D.R. & EDWARDS, S.F. 1982 Spontaneous interparticle percolation. *Proc. R. Soc. A* **381**, 33–51.
- WILLIAMS, S.C. 1968 The mixing of dry powders. *Powder Technol.* **2**, 13–20.
- WILLS, B.A. 1979 *Mineral Processing Technology*. Pergamon.
- XIAO, H.Y., UMBANHOWAR, P.B., OTTINO, J.M. & LUEPTOW, R.M. 2016 Modelling density segregation in flowing bidisperse granular materials. *Proc. R. Soc. A* **472**, 20150856.